Travail de Fin d'Etudes : Characterization of Proton Exchange Membrane fuel cells with catalytic layers of various composition - determination of the cathodic layer limitations

Auteur : Servais, Tom
Promoteur(s) : Job, Nathalie
Faculté : Faculté des Sciences appliquées
Diplôme : Master en ingénieur civil physicien, à finalité approfondie
Année académique : 2019-2020
URI/URL : http://hdl.handle.net/2268.2/10350

Characterisation of Proton Exchange Membrane fuel cells with catalytic layers of various composition – determination of the cathodic layer limitations

Master thesis conducted by

Tom Servais

under the supervision of

Prof. Nathalie Job

with the aim of obtaining the degree of Master in Physical Engineering

Academic year 2019-2020 - University of Liège

ACKNOWLEDGEMENTS

First, I would like to thank my supervisor, Prof. Nathalie Job, for introducing me to the PEM fuel cell field and for giving me the chance to complete this master thesis. Also, I would like to express my thanks for her constructive remarks and her guidance throughout the project.

I would like to thank Aleksandra Grzelak and Fabien Deschamps for sharing their expertise and for the time they devoted to me during the past year.

I would like to thank Prof. Cedric Gommes for his valuable help for the development of the numerical model.

Finally, I want to thank Prof. Benoit Heinrichs and Prof. Tristan Gilet for accepting to be part of the jury and for reviewing this manuscript.

CONTENTS

INTRODUCTION

The proton exchange membrane (PEM) fuel cell is a promising alternative to the current energy converters that work with fossil fuels. Its durability, its ability to work at low temperature and its compactness are valuable qualities that could make this device the future of power sources. Furthermore, the PEM fuel cell does not reject pollutants but only water as a by-product. Despite all the aforementioned advantages, the PEM fuel cell is not yet fully commercialised. The main reason is its high manufacturing cost, due among other factors to the platinum used to catalyse the chemical reactions [1, 2].

A PEM fuel cell is a device that converts chemical energy into an electrical current (Fig. 1). Similarly to a battery, it operates through a pair of redox reactions separated by an electrolyte, the proton exchange membrane. However, the anode and the cathode have to be flushed continuously with fuel (H_2) and oxidant (O_2 through air) respectively to produce electrical energy. At the anode, where the hydrogen oxidation reaction occurs, the fuel is oxidised and delivers protons and electrons:

$$H_2 \rightarrow 2\,H^+ + 2\,e^- \tag{1}$$

The proton exchange membrane allows to transport protons directly to the cathode while being electrically insulating which forces the electrons to reach the cathode *via* the outer circuit. The reaction at the cathode involves the protons and the electrons delivered at the anode as well as the oxidant to make the oxygen reduction reaction:

$$O_2 + 4\,H^+ + 4\,e^- \rightarrow 2\,H_2O \tag{2}$$

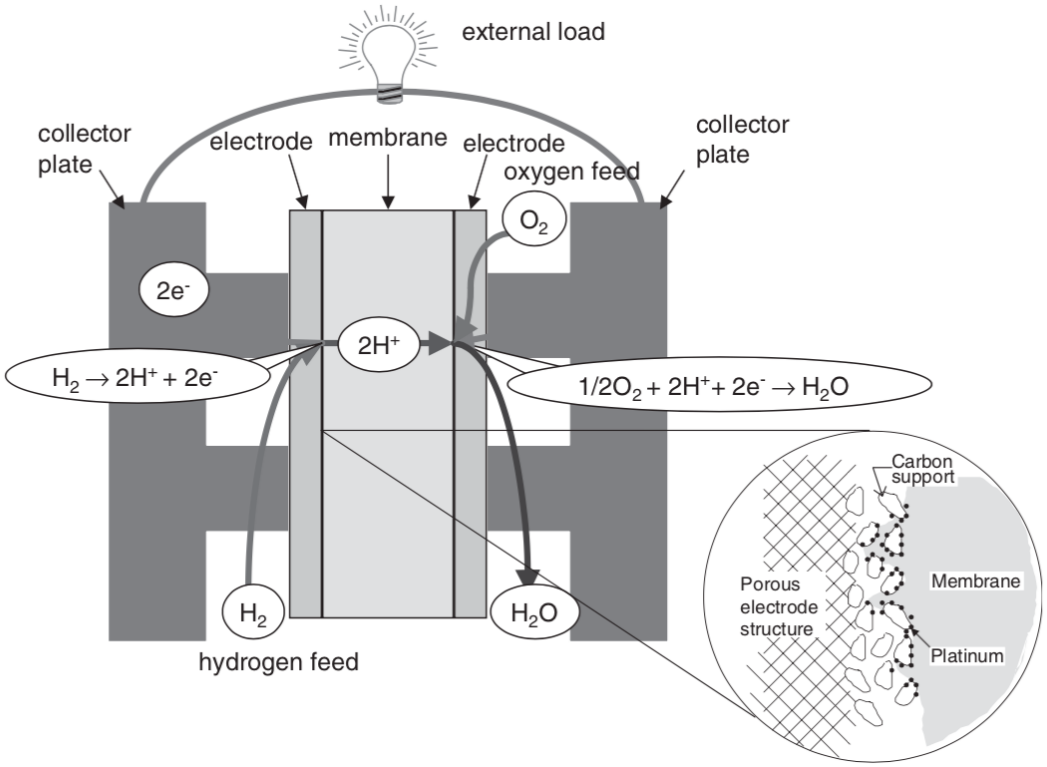

Figure 1: Schematic of a PEM fuel cell and structure of the catalytic layer. [3]

To decrease the amount of Pt inside the device and, therefore, the cost of fabrication, the Pt is dispersed in nanometer-sized particles on a conductive carbon support to form the catalytic layers on each side of the PEM. This configuration provides a high catalyst surface area but necessitates that the chemical reactants have access to each Pt particle. While the electrons are conducted by the carbon, the pores of the support are used to supply the other chemical species. The gas reactants simply diffuse in the carbon structure and a ionomer network is usually built in the pores to make a path for the protons between the PEM and the Pt. The ionomer used is a polymer of the same type as the PEM, and the network is somewhat reconstructed within the catalytic layer during its manufacture.

Using the very general Nernst equation, one can calculate the voltage of the cell in open circuit, *i.e.* when no current circulates in the outer circuit. However, when a current is produced by the PEM fuel cell, three different voltage drops (or overpotentials, η), which corresponds to energy losses, are usually distinguished:

$$\eta = \eta_k + \eta_{ohm} + \eta_{diff} \tag{3}$$

The chemical reactions require a certain amount of energy in order to activate and the voltage of the PEM fuel cell is decreased by η_k. Once this energy barrier is crossed, as the

current starts to increase, the transport of electrons and ions through the ionomer and the carbon support becomes a limiting factor (η_{ohm}). As a result, the cell voltage decreases linearly with the current following Ohm's law. At larger currents, the supply of gas reactants becomes slower than the reaction rate. The diffusion of the gas through the electrode to the active sites causes a further decrease of the cell voltage (η_{diff}). While the activation energy is inherent to the chemical reactions and the choice of catalyst, the overpotentials related to the transport of charges and to the diffusion of gas reactants are sensitive to the electrode structure. However, the voltage losses are seen as "black boxes": for instance, when charge transport is an issue, there is no way to know if the limitation comes from the ion or the electron transport in the system. The same comment can be done regarding oxygen transport *vs.* ion or electron transport. In short, the question is: which of these phenomena is limiting in the process ?

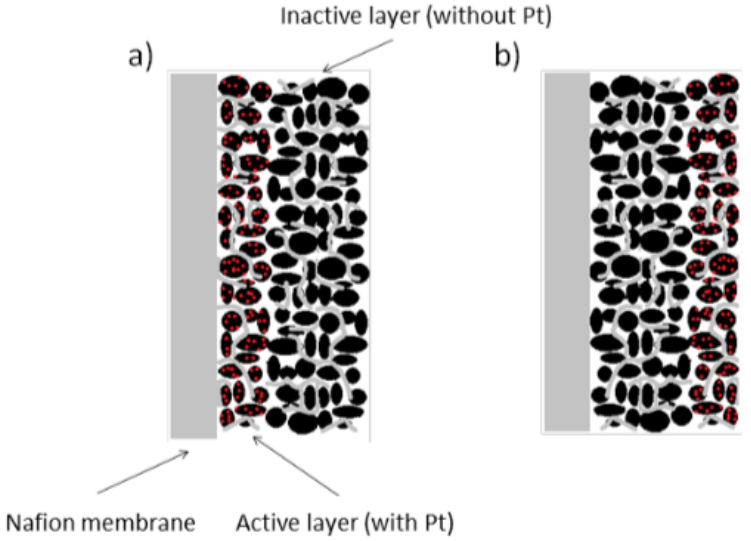

Figure 2: Schematic of the compositions of the catalytic layers envisaged in this master thesis. (a) Configuration in which the Pt is close to the membrane and far from the oxygen and electron supply; (b) configuration in which the Pt is far from the membrane and close to the oxygen and electron supply.

This project aims at studying the origin of the limitations in performance on the cathode side of the PEM fuel cell. In order to discriminate between ion, electron and oxygen transports, different compositions in catalyst could be considered. The configurations to be explored are the cases where the catalyst particles are present only on a portion of the catalytic layer. The contribution of each part of the catalytic layer could be discriminated and the distribution of Pt could be optimised to decrease the overpotential. Fig. 2 displays

the two opposite distributions which we are interested in. In (a), the catalyst is close to the membrane and the distance to be crossed by the protons is small. Oxygen is however forced to diffuse in the whole catalytic layer to reach the active sites and electrons have a longer path to cross to reach platinum. The distribution of catalyst (b) has the opposite effect on the chemical species. The protons have to be conducted across the whole width of the catalytic layer through the ionomer network. The diffusion process that channels oxygen to the active sites is however reduced to a smaller distance while electrons do not need to cross the whole catalytic layer to reach Pt.

Structure of the master thesis

After a review of the PEM fuel cell characteristics and working principles, the synthesis of Pt catalyst on a carbon support is considered (Chapter 2). Pt on carbon black is synthesised using an impregnation technique with formic acid as reducing agent. Subsequently, PEM fuel cells with a constant catalyst composition are manufactured and characterised (Chapter 3). Two conditioning techniques are used to stabilise the PEM fuel cell performance and the degree of reproducibility of the fabrication process is assessed. Unfortunately, the COVID-19 health crisis prevented to continue the experiments at the laboratory and to characterise various compositions of the catalytic layers. The last part of this project is thus dedicated to the development of a 1D model for the cathode catalytic layer (Chapter 4). The transport of the chemical species involved in the oxygen reduction reaction is described in a pseudo-homogeneous catalytic layer. The model is eventually used to evaluate the dependency of the reaction rate with respect to the medium depth and to check under what conditions the typical voltage *vs.* current curve of a PEM fuel cell is obtained.

CHAPTER 1

PEM FUEL CELL FUNDAMENTALS

This chapter is dedicated to the review of the PEM fuel characteristics. The different fuel cell types are first briefly outlined and compared. The components of the PEM fuel cell are then described. Finally, the cell performance and the different sources of voltage losses are tackled.

1.1 Types of fuel cells

A fuel cell is an electrochemical energy converter that uses a fuel to make the oxidation at the anode and an oxidant at the the cathode to perform the reduction. These electrodes are separated by an electrolyte that allows the ions to travel between the two electrodes and prevents an internal shortcut in the device. Different fuel cells are studied based on the type of fuel used in the electrochemical reactions or the type of electrolyte [4]. In the literature, one commonly finds five types of fuel cells: alkaline fuel cells (AFC), phosphoric acid fuel cells (PAFC), molten carbonate fuel cells (MCFC), solid oxide fuel cells (SOFC) and proton exchange membrane fuel cells (PEMFC).

The alkaline fuel cell (AFC) was the first type of device developed in the fuel cell technologies. The first prototype was produced by NASA for the Apollo-series missions. At the anode of the AFC, hydrogen is oxidised and releases water and electrons:

$$\mathrm{H_2} + 2\,\mathrm{OH^-} \rightarrow 2\,\mathrm{H_2O} + 2\,\mathrm{e^-} \tag{1.1}$$

Oxygen is reduced at the cathode to produce hydroxide ions:

$$\mathrm{O_2} + 2\,\mathrm{H_2O} + 4\,\mathrm{e^-} \rightarrow 4\,\mathrm{OH^-} \tag{1.2}$$

The hydroxide ions are transported from the cathode to the anode by the electrolyte made of potassium or sodium hydroxide [5]. This is the main feature that differentiates them from acidic fuel cells like PEM fuel cells. The chemical reactions in AFCs have the advantage to be relatively fast even on low-cost catalysts such as nickel or silver, which leads to reasonable losses due to kinetic overpotential. However, the electrolyte is easily poisoned by CO_2 molecules which forces a high purity of the gas reactants. As H_2 is usually produced by steam methane reforming and O_2 is drawn from the ambient air, this condition cannot be easily met. Moreover, the device is inconvenient due that the fact that the electrolyte is liquid. Alkaline membranes are nowadays studied in the literature to overcome this problem [6].

Phosphoric acid fuel cells (PAFC) work with the same chemical reactions as the PEM fuel cells, as described in the introduction; the hydrogen oxidation reaction at the anode:

$$\mathrm{H_2} \rightarrow 2\,\mathrm{H^+} + 2\,\mathrm{e^-} \tag{1.3}$$

and the oxygen reduction reaction at the cathode:

$$\mathrm{O_2} + 4\,\mathrm{H^+} + 4\,\mathrm{e^-} \rightarrow 2\,\mathrm{H_2O} \tag{1.4}$$

The differences between the two devices are the use of phosphoric acid (H_3PO_4) dispersed in a silicon carbide matrix as the electrolyte and the higher operating temperature of the device (approximately 473 K *vs.* 343 K for PEMFCs). The major drawback of this technology is that it is adapted to large stationary applications only due to the long warm-up procedure and the risk of electrolyte freezing at room temperature. Also, like PEM fuel cells, the Pt catalyst used is sensitive to CO poisoning.

The molten carbonate fuel cell (MCFC) principle is based on the reaction between hydrogen and carbonate ions:

$$\mathrm{H_2} + \mathrm{CO_3^{2-}} \rightarrow \mathrm{H_2O} + \mathrm{CO_2} + 2\,\mathrm{e^-} \tag{1.5}$$

The cathode reaction involves oxygen, carbon dioxide and electrons:

$$2\,\mathrm{CO_2} + \mathrm{O_2} + 4\,\mathrm{e^-} \rightarrow 2\,\mathrm{CO_3^{2-}} \tag{1.6}$$

Carbonate ions travel from the cathode to the anode by the electrolyte made of molten carbonate and alkaline metals, usually lithium and potassium (Li_2CO_3/K_2CO_3) [5]. Because the electrolyte needs to be in liquid phase to operate, the temperature of the device is about 873 K. The reactions in MCFCs coupled with the high operating temperature allow to resist to CO and CO_2 poisoning and to use directly CH_4 as a fuel. The device is nevertheless not

completely "green" in that case as it requires and rejects CO_2, which is ideally recycled. The other drawbacks of MCFCs are that it is suitable for stationary applications only and the electrolyte is subject to corrosion.

Another fuel cell type is the solid oxide fuel cell (SOFC). The ions in such cells are O^{2-} produced at the cathode:

$$O_2 + 4\,e^- \rightarrow 2\,O^{2-} \tag{1.7}$$

Those ions reacts with the hydrogen at the anode to produce water:

$$H_2 + O^{2-} \rightarrow H_2O + 2\,e^- \tag{1.8}$$

The electrolyte is a layer of ceramic usually composed of stabilised zirconia material that exhibits a good ionic conductivity at very high temperature (873 K to 1273 K).

Finally, the PEM fuel cells shortly described in the introduction are the most promising fuel cell devices. This type of device works at relatively low operating temperature (343 to 363 K) thanks to its membrane electrolyte. Their warm-up procedure is fast, whatever their size, and the electrolyte is a solid polymer membrane. Furthermore, PEM fuel cells can be used in different applications [7]: portable devices, transportation or stationary systems. However, the Pt to catalyse the reactions is an expensive material, which is one of their main drawbacks. PEM fuel cells are fully described in the next section.

1.2 PEMFC components and working principles

As any electrochemical generator, a PEMFC is composed of two electrodes separated by one electrolyte. The most used material for the electrolyte, the proton exchange membrane, is made of perfluorosulfonic acid/ tetrafluoroethylene copolymer, also named Nafion® [8]. Apart from being a reactant barrier and preventing an internal shortcut, the advantages of this compound are its good proton conductivity, its good mechanical properties and its resistance to both oxidation and reduction thanks to its Teflon® backbone [9]. The ionic conductivity is nevertheless highly dependent on the water content of the membrane. This is the reason why the fuel and oxidant have to be supplied with high relative humidity [10]. The membrane usual thickness can go from 50 μm for Nafion® 212 to 183 μm for Nafion® 117. Attempts to decrease the thickness have led to cells with lower resistance, but also with lower lifetime due to mechanical breakage.

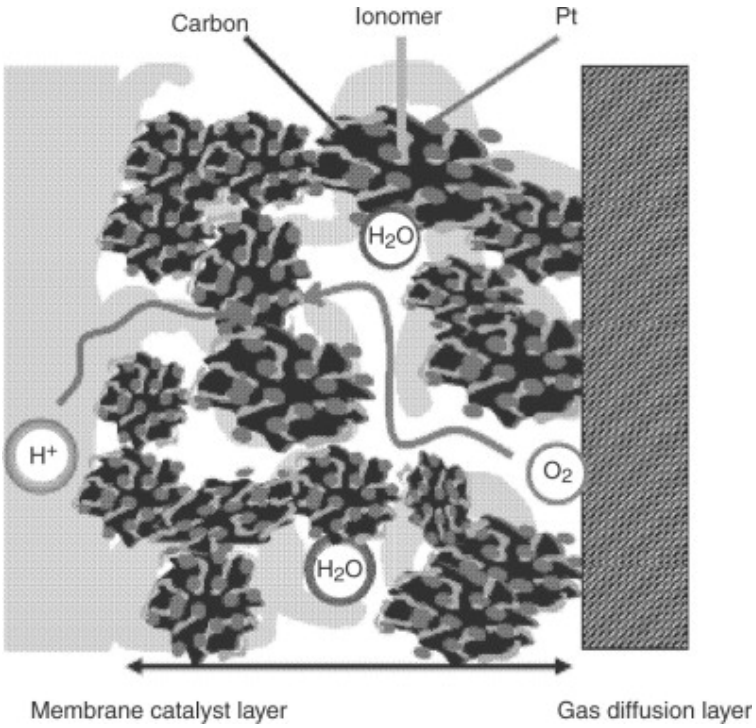

Figure 1.1: Catalytic layer structure inside the cathode of the PEM fuel cell. [11]

The electrochemical reactions in the PEM fuel cell are catalysed by Pt or Pt-alloy on both the anode and the cathode. The active sites are spread on a porous carbon support to maximise the number of active sites per unit volume of the electrode. [12] Nafion® is also added as a binder and ionic conductor to form the catalytic layers on each side of the PEM ($\sim$10 μm) (Fig. 1.1). This part of the electrode has multiple properties [9]:

- porosity for hydrogen (at the anode) and oxygen (at the cathode) to reach the catalyst;
- proton conductivity between the catalyst and the PEM;
- electronic conductivity between the catalyst and the outer circuit.

The catalyst sites thus need a triple contact between Pt, C and Nafion® to form an active site and accessibility of the reactant to the active site through the pore network. The carbon provides electronic conductivity while Nafion® conducts the protons. The ratio in weight of these two compounds has to be carefully chosen in order to provide enough void for the gas supply while ensuring good electric and ionic conductivities [13].

Gas diffusion layers (GDL) are situated next to the catalytic layers. The GDL is generally composed of two sub-layers. The main sub-layer is macroporous and electrically conductive, usually carbon cloth or carbon paper (200-400 μm). It allows to collect the electrons, provide

a uniform gas feed and homogenise the pressure on the catalytic layer. The second sub-layer close to the active sites is a thin micro-porous hydrophobic carbon layer (∼50 μm) [8]. Its role is to remove the water produced from the ORR directly at the cathode or at the anode through the membrane. It prevents the catalytic layer from flooding by the water produced [14].

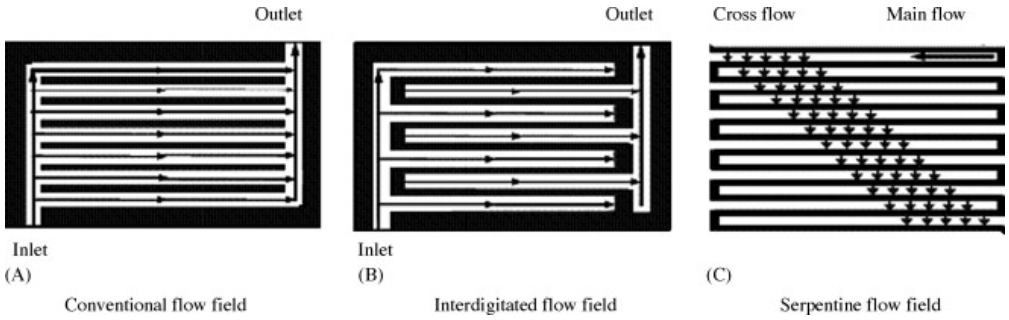

Figure 1.2: Plane view of bipolar plates highlighting different flow channels architectures. [14]

Finally, the last significant parts of a PEM fuel cell are the bipolar plates. They are usually made of graphite, stainless steel or coated metal to avoid corrosion. They contain the inlet and outlet holes for the reactants and they supply the gas to the GDLs on both side of the fuel cell. The bipolar plate has two main functions: (i) carry the current away from the cell, and (ii) distribute the flow of gas reactant to the electrode [15]. Many parallel flow channels connect the two holes in order to uniformly distribute the fuel or oxidant. The geometry of the channels in the plates is variable and is a current hot research topic (Fig 1.2).

1.3 Open circuit voltage

At equilibrium, the theoretical potential E for a redox reaction at one electrode:

$$\mathrm{Ox} + \mathrm{n\,e^-} \leftrightharpoons \mathrm{Red} \tag{1.9}$$

is given by Nernst equation:

$$E = E_0 + \frac{RT}{nF} \ln\left(\frac{p_O}{p_R}\right) \tag{1.10}$$

where E_0 is the standard potential, R is the perfect gas constant, T is the temperature, n is the number of electrons transferred in the reaction, F is the Faraday constant and p_O, p_R are the partial pressures of the oxidised and the reduced form respectively. Applying this

equation to both electrodes of the PEM fuel cell gives the theoretical open circuit voltage (OCV) E_{Nernst}, *i.e.* the voltage when no current is delivered by the cell:

$$E_{Nernst} = E_c + E_a \tag{1.11}$$

with c and a being the subscripts for cathode and anode [16]. When developing the two terms for the hydrogen oxidation reaction at the anode:

$$\mathrm{H_2} \rightarrow 2\,\mathrm{H^+} + 2\,\mathrm{e^-} \tag{1.12}$$

and the oxygen reduction reaction at the cathode:

$$\mathrm{O_2} + 4\,\mathrm{H^+} + 4\,\mathrm{e^-} \rightarrow 2\,\mathrm{H_2O} \tag{1.13}$$

the equation for E_{theor} becomes:

$$E_{Nernst} = E_{0,c} + \frac{RT}{4F} \ln[p(\mathrm{O_2})\,(p(\mathrm{H_2}))^2] \tag{1.14}$$

with $E_{0,a} = 0$ V by convention and the water produced assumed to be liquid [12]. The theoretical value for the OCV is 1.229 V at 298 K and with pure H_2/O_2 at ambient pressure.

In practice, the PEM fuel cell never reaches E_{Nernst} even with no net current produced. It is due to H_2 crossover and mixed potential [17]. Indeed, a portion of the H_2 injected at the anode crosses the PEM and is oxidised at the cathode. Also, Pt catalyst particles are not stable on the cathode side at potential close to E_{Nernst} and are partially oxidised with the following reaction:

$$\mathrm{Pt} + \mathrm{H_2O} \rightarrow \mathrm{PtO} + 2\,\mathrm{H^+} + 2\,\mathrm{e^-} \tag{1.15}$$

Moreover, carbon is oxidised at this electrode potential. Thus, four reactions occur at the cathode: Pt and C oxidations, HOR and ORR. The practical open circuit voltage E_{OCV} reported in the literature is thus closer to 1 V due to that mixed potential.

1.4 Overpotential

The open circuit voltage E_{OCV} previously described is the cell voltage when no current is delivered by the PEM fuel cell. When one wants to generate power from the device, the cell voltage E gets lower as the current increases. The cause for the voltage drop or overpotential

$$\eta = E - E_{OCV} \tag{1.16}$$

is commonly attributed to three factors [3, 12]: (i) the kinetics of the reactions (η_k), (ii) the ohmic resistance of the device (η_{ohm}) and (iii) the mass transport, *via* the diffusion of

the reactants inside the electrodes (η_{diff}). The typical current density/cell potential plot or polarisation curve for a PEM fuel cell is represented in Fig. 1.3 and shows the dependence of the overpotential to the three aforementioned factors [12]:

$$\eta = \eta_k + \eta_{ohm} + \eta_{diff}. \tag{1.17}$$

Note that, as the cell voltage E decreases when the current I increases, the power delivered by the PEM fuel cell:

$$P = E\,I \tag{1.18}$$

exhibits a maximum between 0.6 and 0.7 V. Therefore, the operating voltage for the device is usually around these aforementioned values

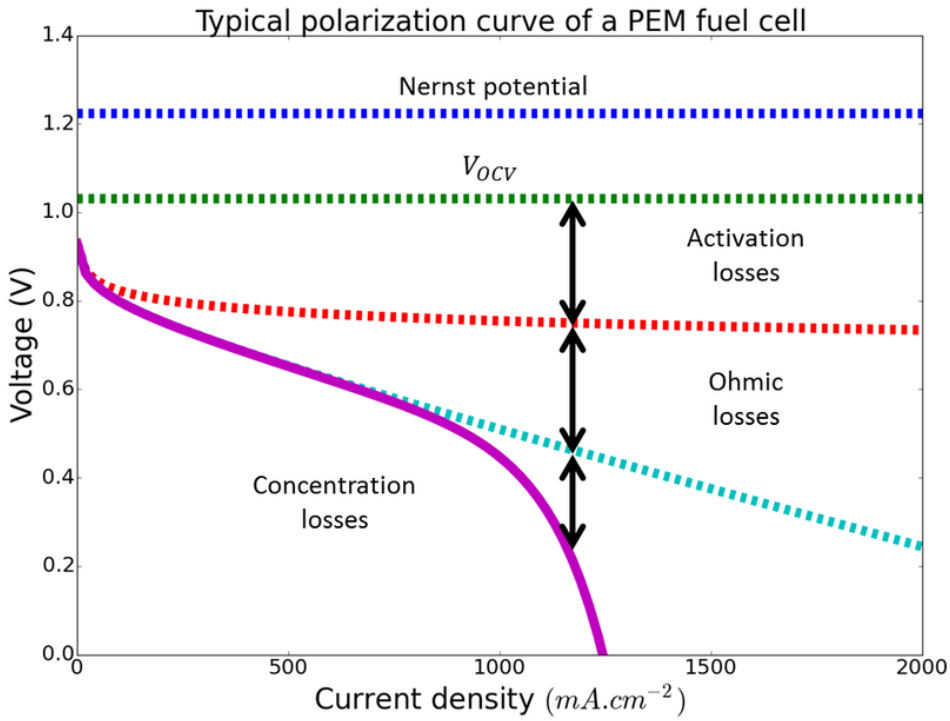

Figure 1.3: PEM fuel cell polarisation curve. [3]

1.4.1 Kinetic loss

The relation between the current and the kinetic potential drop for a redox reaction at one electrode:

$$\mathrm{O} + \mathrm{n\,e^-} \underset{\text{backward}}{\overset{\text{forward}}{\rightleftharpoons}} \mathrm{R} \tag{1.19}$$

is given by the Butler-Volmer equation:

$$i = i_0 \left(\frac{C_{ox}}{C^0_{ox}} \exp\left[\frac{\alpha\, n_\alpha\, F\, \eta}{R\, T} \right] - \frac{C_{red}}{C^0_{red}} \exp\left[-\frac{(1-\alpha)\, n_\alpha\, F\, \eta}{R\, T} \right] \right) \tag{1.20}$$

where i is the current, i_0 is the exchange current, α is the transfer coefficient, n_α is the electron transfer number, C and C^0 are associated to the concentrations at the electrode surface and far from the electrode, ox and red are subscripts for oxidants and reductants. F is the Faraday constant, R is the gas constant and T is the temperature. α is a constant related to the symmetry of the energy barrier [16]. It takes a value between 0 and 1 and it is equal to 0.5 for the ORR and HOR [18]. As the Butler-Volmer equation accounts for a reaction with the exchange of one electron, n_α is introduced in the exponential factor for reactions involving more than one electron exchanged. n_α differs from the number of electrons transfered n in Nernst equation. Its value is 2 for the HOR and can be 1 or 2 depending on the cathode potential for the ORR [18]. The two terms into brackets of Eq. 1.20 correspond to the forward and backward redox reactions at one electrode and their associated current can be written as:

$$i_f = i_0 \left(\frac{C_{ox}}{C^0_{ox}} \exp\left[\frac{\alpha\, n_\alpha\, F\, \eta}{R\, T} \right] \right) \tag{1.21}$$

$$i_b = -i_0 \left(\frac{C_{red}}{C^0_{red}} \exp\left[-\frac{(1-\alpha)\, n_\alpha\, F\, \eta}{R\, T} \right] \right). \tag{1.22}$$

where f and b subscripts stand for forward and backward, respectively.

When talking about a cell with two redox reactions and two electrodes, the anodic and cathodic currents are both given by the Butler-Volmer relation and are always equal

$$i_a = i_c \tag{1.23}$$

The associated cell overpotential or drop in performance can be written as the sum of the contribution from each electrode:

$$\eta = \eta_a + \eta_c. \tag{1.24}$$

At the open circuit voltage ($\eta = 0$), when both electrodes are at equilibrium (*i.e.* their Nernst potential), no net current is produced. Nevertheless, an exchange of electrons still occurs on both the anode and the cathode. This current is equal for the backward and forward reactions and is named the exchange current i_0. In the case of the HOR and ORR occuring in the PEM fuel cell, i_0 is two orders of magnitude smaller for the latter reaction [18]. A smaller value of i_0 means that a larger overpotential is needed in order to activate the reaction and deliver a net current i. In practice, the kinetic loss in a PEM fuel cell is

thus attributed to the cathode reaction only as $\eta_a << \eta c$.

When overtaking this kinetic loss and reaching larger currents, the effect of the backward reaction in the Butler-Volmer relation can be neglected and the low-current polarisation curve, *i.e.* the portion of the curve where the reaction rate does not affect the concentration of reactants in the cell ($C_{ox} = C^0_{ox}$) is generally described using the so-called Tafel equation [16] applied to the ORR of the cathode electrode:

$$i = i_{0c} \left(\exp \left[\frac{\alpha_c \, n_{\alpha c} \, F \, \eta}{R \, T} \right] \right) \tag{1.25}$$

The kinetic loss is:

$$\eta_k = a + b \, \log(i) \tag{1.26}$$

where:

$$a = \frac{2.3 \, R \, T}{\alpha_c \, n_{\alpha c} \, F} \log(i_{0c}) \qquad b = -\frac{2.3 \, R \, T}{\alpha_c \, n_{\alpha c} \, F}. \tag{1.27}$$

1.4.2 Ohmic loss

At higher current, the ohmic loss becomes significant with the emergence of a linear slope in the polarisation curve (Fig. 1.3). This ohmic overpotential is expressed as

$$\eta_{ohm} = R_i \, i \tag{1.28}$$

with R_i being the internal resistance of the PEM fuel cell. R_i includes mainly (i) the resistance due the PEM, (ii) the contacts between each component of the device and also (iii) the electronic resistance which is usually negligible [3].

1.4.3 Diffusion loss

When the current increases, the oxygen consumption gets faster in the electrode. As a result, the concentration of gas reactant inside the catalytic layer becomes smaller than the inlet concentration of the fuel cell. The catalytic layer is depleted of reactant as the diffusion process inside this porous material hinders the gas transport to the active sites [3].

Going back to Eq. 1.20, the reactant concentration issue is introduced with the C/C^0 factors before the exponential terms. However, the actual concentration of reactant inside the catalytic layer cannot be retrieved experimentally and prevents the development of an analytic expression for the diffusion voltage loss η_{diff} and the whole polarisation curve. Different empirical models are reported in the literature [19, 20] where the diffusion overpotential is retrieved from the fit and the subtraction of the kinetic and ohmic overpotentials. Even

though those models give a perfect fit for the polarisation curve, it does not provide any insight into the concentration and diffusion loss of the PEM fuel cell.

In Fig. 1.4a, PEM fuel cells were manufactured with gas diffusion layer fabricated with different techniques [21]. As a result, the porosity of the components is varied and the water management in the electrode implies different diffusion losses. Similarly, the Nafion® content is changed in the catalytic layer (Fig. 1.4b). For a too small amount of Nafion®, the ionomer cannot play its conducting role. On the contrary, a high Nafion® content blocks the carbon pores and the gas supply to the catalyst. Those examples of the diffusion overpotential show that multiple parameters can be responsible for a decrease of the performance.

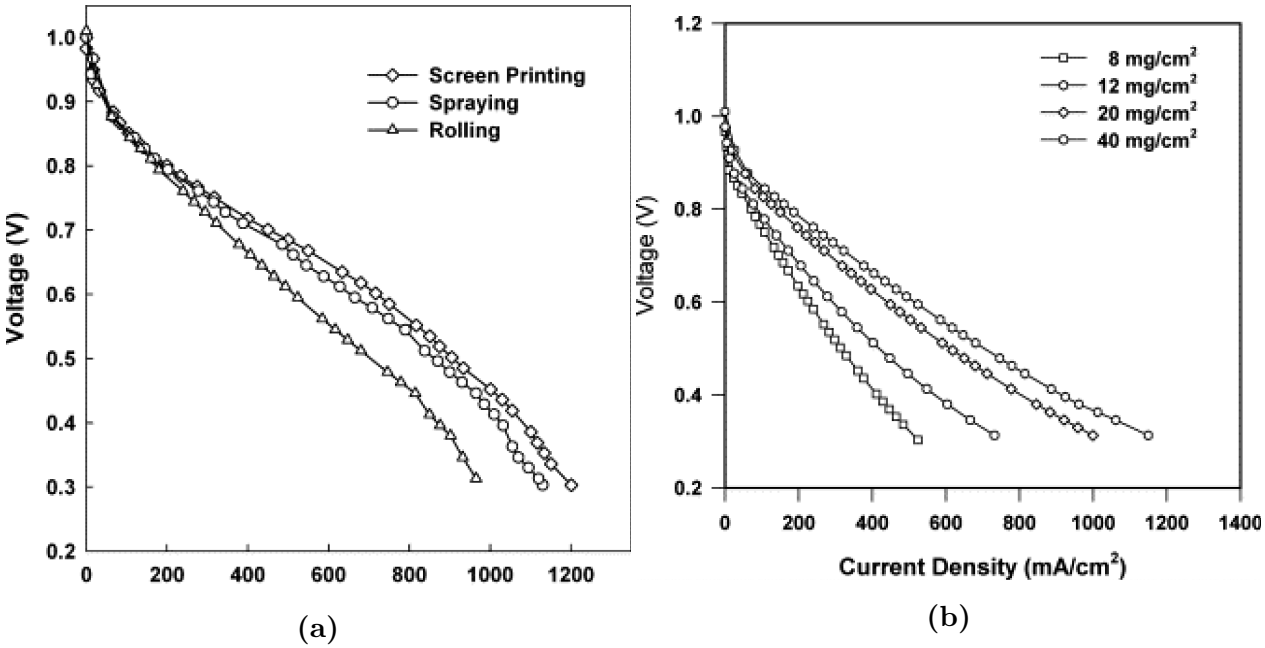

Figure 1.4: Polarisation curves for different gas diffusion layer fabrication techniques implying different porosity (a) and for different Nafion® content in the catalytic layer (b). [21]

1.5 Conclusion

In this review of the PEM fuel cell, the role of each component was described. Moreover, the different factors impacting the performance of the device were outlined. The present work aims at determining how each part of the catalytic layer, *i.e.* the medium where the chemical reactions are catalysed, is impacted by the cell voltage drops or overpotentials in

order to, later, increase its efficiency. While the active surface area is optimised by synthesising smaller particles to reduce the cost of the device, knowing how each part of the catalytic layer works would allow to optimise the distribution of catalyst and further decrease the cost. The following chapters of this master thesis are dedicated to the implementation of membrane-electrodes assemblies and to the spatial dependence of the overpotential inside the cathodic catalytic layer of the PEM fuel cells.

CHAPTER 2

ELECTROCATALYST SYNTHESIS AND CHARACTERISATION

2.1 Introduction

One of the current challenges encountered in the field of fuel cells is the diminution of the amount of Pt inside the catalytic layer while maintaining a high power density. Indeed, the use of this catalyst increases the cost of the device and limits its commercialisation. Several strategies were investigated to counter this drawback including an optimised dispersion of Pt and the development of more active Pt-alloy electrocatalysts [22].

Dispersing the catalyst consists in synthesising smaller Pt particles to reach a larger surface area per weight of catalyst and thus increase the number of active sites. However, the activity of Pt for the oxygen reduction reaction occurring in the PEM fuel cell is structure-sensitive. When smaller particle sizes are reached, more active sites are situated on the edges of the Pt particles where the intermediate products of the ORR are more strongly bound. As a result, the kinetics of the ORR tend to decrease for smaller catalyst particle sizes. The optimal Pt particle size is of the order of 3 to 4 nm for the best performance of the fuel cell as it maximises the mass activity, *i.e.* the current per unit mass of Pt [23, 24].

A common choice for the carbon support is carbon black. This support is easily available as it is produced by thermal decomposition of hydrocarbons; it is widely used as ink pigment or as additive to improve the mechanical properties of rubber in the tire industry. Carbon black is composed of microporous near-spherical particles with sizes of the order of 10 to 400

nm. This leads to a large surface area and the presence of pores in the range of 10 to 20 nm while maintaining a proper electron conductivity. The large surface area allows to disperse the catalyst particles. The pore texture is used to build the Nafion® network and diffuse the reactants and products. Finally, the carbon has to supply electrons to the active sites. [25]

Many different methods to obtain Pt nanoparticles on a carbon support are described in the literature. These methods include (i) deposition from the gas phase using thermal vapour deposition or metal sputtering and (ii) deposition from liquid phase based on the colloidal synthesis, the electrodeposition or the impregnation. [25]

In this project, the synthesis of catalyst is approached for the purpose of making PEM fuel cell catalytic layers with various compositions. Pt deposited on carbon black is prepared using a one-step synthesis: the direct impregnation-reduction in liquid phase with formic acid as reductant. This method was previously developed at the laboratory on a different carbon support [26] and the obtained catalysts were compatible with an utilisation in fuel cells. The Pt/C powders are then characterised with physical and electrochemical methods in order to verify the nature of the products and evaluate their catalyst particle size and activity prior to electrode manufacturing.

2.2 Experimental

2.2.1 Synthesis

The synthesis route utilised for this project is the easy-to-implement impregnation using formic acid (HCOOH) as a reducing agent. It consists in reducing a Pt salt ($H_2PtCl_6.6H_2O$) in liquid phase on a carbon support (C black). Four different batches numbered from 1 to 4 were made to check the reproducibility of the synthesis technique. In order to compare the synthesised powders with a commercial Pt/C black catalyst (Premetek P10A200), the composition was chosen as 20 wt. % of Pt. The experimental setup is displayed in Fig. 2.1 and the procedure is the following [27, 26]:

- 0.3 g of XC-72R carbon black (Cabot) are dispersed in 200 mL of 2 mol L^{-1} formic acid (HCOOH) solution using a magnetic stirrer;
- the solution is heated to 333 K in an oil bath;

- 100 mL of 4 mmol L^{-1} of $H_2PtCl_6.6H_2O$ are integrated into the solution by steps of 10 mL;
- the solution is filtered after 1 h stirring using a Buchner funnel and washed 5 times with 125 mL of MilliQ water;
- the obtained powder is dried overnight under air at 323 K.

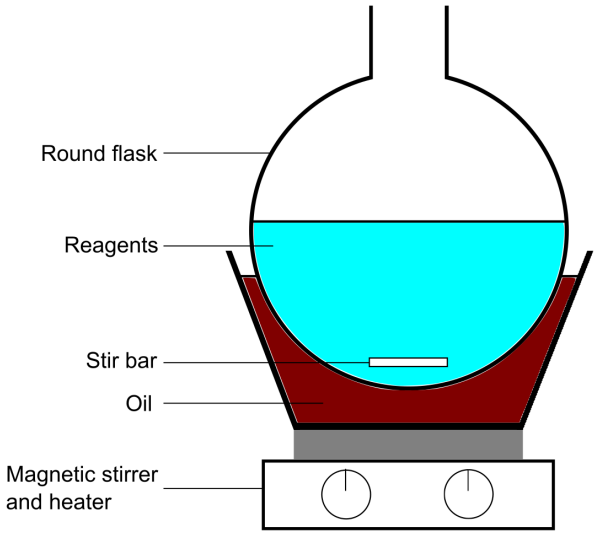

Figure 2.1: Schematic of the experimental setup used for the impregnation using formic acid synthesis.

2.2.2 Physical characterisation

X-ray diffraction (XRD)

X-ray Diffraction is a non-destructive method that allows to determine the chemical composition of a crystal. This technique is based on the scattering of an X-ray beam by the atomic electrons of the crystal to be characterised. Indeed, for a lattice spacing of the same order of the wavelength of the X-rays, the beams scattered by different atomic planes interfere with each other. These interferences then give rise to maxima and minima according to Bragg's law. The resulting pattern is specific to the crystallographic arrangement of the material and thus to its chemical composition. [12, 16]

The output given by the XRD is the intensity of the scattered X-ray as a function of the diffracted angle. Paul Scherrer noticed that the peaks corresponding to the maxima of interferences is broadened when the size of the coherently diffracting domains or crystallites is shrunk. He derived the relation between these two quantities:

$$d_{XRD} = \frac{K\,\lambda}{B\,\cos(\theta)} \tag{2.1}$$

where d_{XRD} is the crystallite size, $K = 0.89$ is the Scherrer constant for spherical particles, λ is the wavelength of the incident X-ray, B is the full width at half maximum of the peak (FWHM) and θ is the position of the peak in the diffractogram. [12, 28]

The XRD was performed with a Siemens D5000 goniometer using the $Cu_{K\alpha}$ line (Ni filter). The crystallite sizes d_{XRD} were obtained by fitting a Gaussian function on a diffraction peak in order to retrieve the FWHM. Those fittings were made on the larger peaks with the aim of reducing the error.

Transmission electron microscopy (TEM)

The synthesised catalysts were observed with a Jeol 2010 transmission electron microscope (200 kV, LaB_6 filament). The Pt/C powders to be imaged were deposited on millimeter-sized copper grids previously soaked in ethanol. Those copper grids were then clamped into the rod-shaped specimen holder and could be inserted in the vacuum chamber of the TEM. The Pt particle diameters were measured by contrast analysis using the ImageJ software. In principle, to get reliable results, the measurement should be performed on at least 100 particles (assuming that the analyzed sample area is representative of the whole material).

2.2.3 Electrochemical characterisation

In a PEM fuel cell, two half electrochemical reactions occur near each electrode. For the next characterisation techniques, namely CO Stripping and Rotating Disk Electrode (RDE), the experimental setup consists in simulating one side of the fuel cell. This half-cell setup is commonly composed of three electrodes (Fig. 2.2) [26]. The working electrode (WE) is made of a disk of glassy carbon surrounded by a Teflon sheath and connected to a rotating motor. The counter electrode (CE) is a Pt wire ended by a Pt mesh. As a current is produced, an overpotenial modifies the potential of the CE. This effect prevents the CE potential to be used as a reference potential. The potential of the WE is thus imposed with respect to an isolated reference electrode: a normal hydrogen electrode (NHE). Those three electrodes

are immersed in an electrolyte composed of perchloric acid (0.1 M $HClO_4$) which allows to transport the ions. Gas can be bubbled in the electrolyte *via* a gas inlet to purge the solution or to get the reactants for the specific reactions considered.

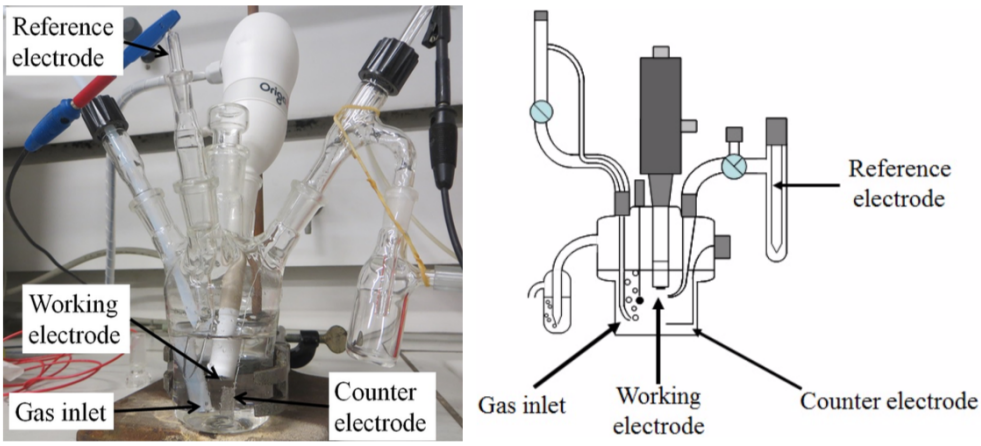

Figure 2.2: (a) Picture and (b) schematic of the three-electrode half-cell set-up.

To perform the experiments, an equivalent catalytic layer had to be deposited on the WE. Inks were prepared with the following composition: 18.3 mg of the Pt/C powders, 3.6 mL of Milli-Q water, 86.4 mg of 5% of Nafion® solution and 1.4 mL of isopropyl alcohol. The mixtures were homogenised by sonication for 15 min. 10 μL of the inks were dropped on the glassy carbon disk of the WE. After evaporation of the solvent, a drop of the electrolyte was deposited on the layer of catalyst and the WE was placed under vacuum for 15 min. This enabled the outgassing of the catalytic layer and improved the wetting between the catalyst and the electrolyte [26].

CO stripping

The CO stripping voltammetry is a technique allowing to measure the electrochemical surface area, *i.e.* the active surface area of catalyst per unit mass. The method is based on the adsorption and electrooxidation of CO molecules on the Pt catalyst surface. The electrolyte is first saturated with CO by bubbling at a fixed WE potential. In that configuration, CO acts like a poison for the catalyst and covers the entire surface of the Pt particles. An inert gas is then bubbled to remove any residual CO molecules in the liquid solution. A linear potential sweep is finally performed and the carbon monoxide that is adsorbed on the Pt is electrooxidised:

$$CO + H_2O \rightarrow CO_2 + 2\,H^+ + 2\,e^- \tag{2.2}$$

This reaction results in a production of electrons and a current peak proportional to the Pt surface area in the voltammogram.

The experimental procedure is the following. A potential of 0.1 V *vs.* NHE is applied to the WE and gaseous CO is bubbled in the electrolyte for 6 min. The electrolyte is purged with Ar for 39 min to remove the oversupply of CO. The CO molecules on the Pt surface are then removed by cycling the potential from 0.05 to 1.23 V *vs.* NHE at 20 mV s^{-1}. Two more cycles with the same parameters are performed subsequently. A peak appears on the voltammogram for the first cycle due to the electrooxidation of the CO and it can be isolated by subtracting the third cycle. [26] The Pt surface area S_{CO} (m^2 g_{Pt}^{-1}) can be computed using:

$$S_{CO} = \frac{S_{peak}}{v_{scan}\, m_{Pt}\, C_{CO}} \tag{2.3}$$

where S_{peak} (A V) is the surface of the peak extracted from the cyclic voltammetry, v_{scan} (V s^{-1}) is the scan speed, m_{Pt} (g) is the mass of Pt on the WE and C_{CO} (= 420 10^{-2} C m^{-2}) is the charge per unit surface necessary to electrooxidise a full mono-layer of CO on a Pt surface [12]. An equivalent Pt particle diameter d_{CO} (m) can be calculated from the catalyst specific surface area [29]:

$$d_{CO} = \frac{6\ 10^{-3}}{S_{CO}\ \rho_{Pt}} \tag{2.4}$$

with ρ_{Pt} (kg m^{-3}) being the density of Pt. Furthermore, the position of the electrooxidation peak is also related to the Pt particle sizes. Pt diameters smaller than 2 nm are responsible for a peak near 1 V *vs.* NHE while Pt particles larger than 3 nm produce a peak at 0.8 V *vs.* NHE. The presence of Pt aggregates in the catalyst powders produce a peak at lower potential (0.75 V *vs.* NHE).

Another feature of this method is that it is possible to verify the amount of catalyst deposited on the WE. Indeed, the Pt particles undergo no modification of their surface around 0.4 V *vs.* NHE and no oxidation or reduction peaks are drawn on the voltammograms. Nevertheless, there is a difference in current between the positive and the negative scan of the cycle in this potential region. This arises from the charge-discharge of the carbon black substrate inside the catalytic layer which acts as a capacitor [12]. A thicker layer would thus lead to a larger capacitive current near 0.4 V *vs.* NHE and a thinner layer would have the opposite effect.

Oxygen reduction reaction on rotating disk electrode (RDE)

The second electrochemical method is used to measure the activity of the catalyst for the oxygen reduction reaction (ORR). RDE experiments consist in saturating the electrolyte solution in oxygen to provide reactant for the reaction and decreasing the potential of the WE from the Nernst potential to a lower value. Due to the slow kinetics of the reaction [18], the current is not produced right below the Nernst potential. The potential of the WE needs to be decreased by the high kinetic overpotential of the ORR. After overtaking this potential barrier, the current increases with the decrease of the potential until reaching a plateau. Indeed, the reaction rate is then limited by the diffusion film through which the oxygen travels to the WE. This mass transfer limitation can be decreased by increasing the rotating speed of the WE as it allows to shrink the diffusion film. The RDE measurements are usually performed with several rotating speeds: the kinetic part of the curve at high potential is overlapped while the limiting current at lower potential is increased with larger rotating speeds. The activity of the catalyst is retrieved from the Koutecky-Levich equation introduced below.

The experimental procedure is described hereafter. Oxygen is bubbled in the liquid electrolyte of the half-cell setup for 15 min. The current is recorded while cycling the potential of the WE from 0.4 to 1.09 and again to 0.4 V *vs.* NHE at 2 mV s^{-1}. Those measurements are performed with rotating speeds of the WE of 1600 rpm and 2500 rpm. [26] The kinetic current i_k, that means the current without the diffusion limitation, can be computed with the Koutecky-Levich equation [16]:

$$\frac{1}{i_k} = \frac{1}{i} - \frac{1}{i_l} \tag{2.5}$$

where i is the current measured experimentally at 0.9 V *vs.* NHE and i_l is the mass transfer limiting current depending on the rotation speed of WE [30]. The average of those kinetic currents obtained for the different rotating speeds is divided by the catalyst surface areas to get the specific activities of the catalysts, SA, at 0.9 V *vs.* NHE. Similarly, those currents can be divided by the mass of catalyst that coats the electrode to obtain the mass activities, MA, at 0.9 V *vs.* NHE.

2.3 Results and discussion

The diffractograms of the four obtained catalysts are displayed in Fig. 2.3. They are compared to the diffractogram obtained using the reference commercial catalyst (Premetek P10A200). Each pattern displays the three peaks related to Pt: at angles 39.7°, 46.2° and 67.5° corresponding to Pt(1 1 1), Pt(2 0 0) and Pt (2 2 0) facets respectively [31]. The average crystallite sizes for the four batches and the commercial catalyst are computed using Scherrer

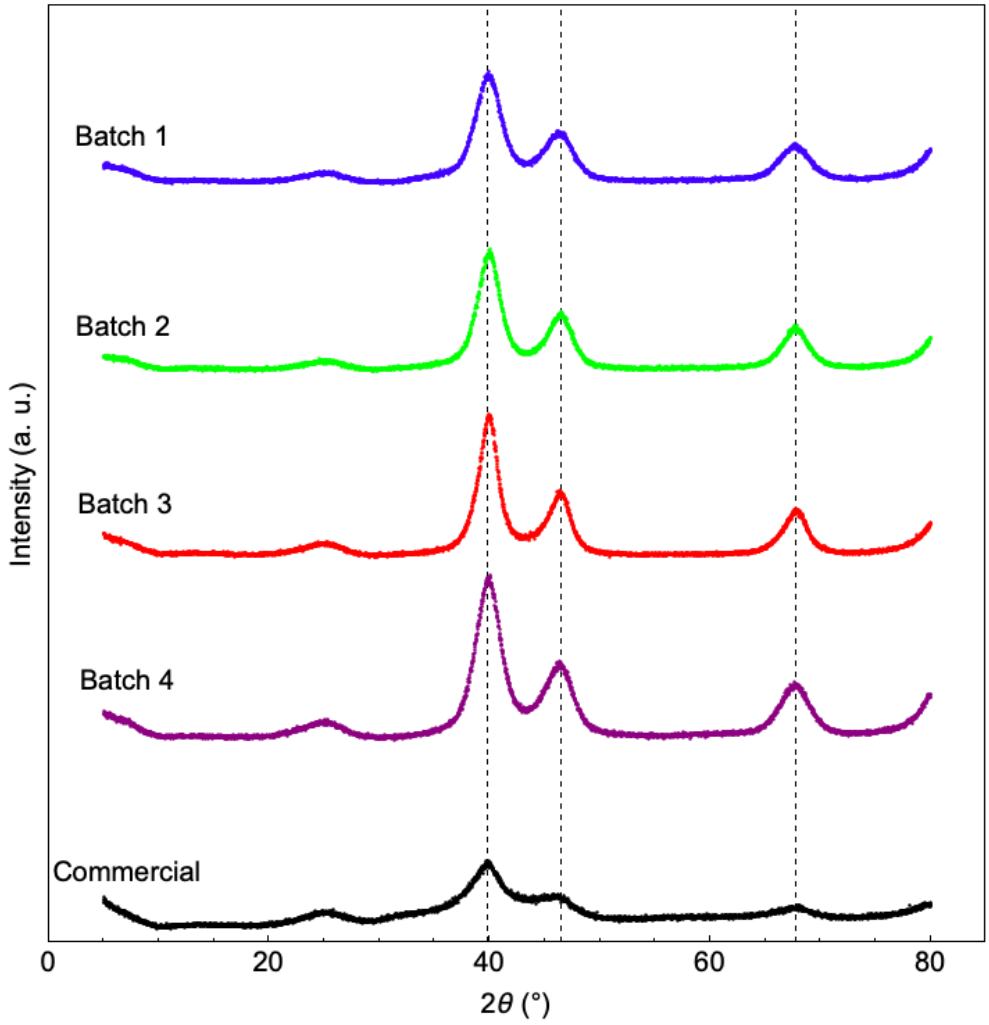

Figure 2.3: Diffraction patterns for the four batches synthesised at the laboratory and the commercial catalyst. The intensity of the peaks are plotted as a function of the diffracted angle 2θ.

Examples of images collected for the four catalyst batches are displayed in Fig 2.4. The denser Pt particles are darker and fixed on the greyish carbon black substrate which has sizes of the order of 100 nm. The Pt particle diameters are of the order of 1 to 10 nm and were reported in histograms in Fig. 2.5. Note that too low amount of particles were used to establish the histograms: the health crisis prevented from obtaining enough data. The number of particle sizes collected is of the order of 100 for each batch.

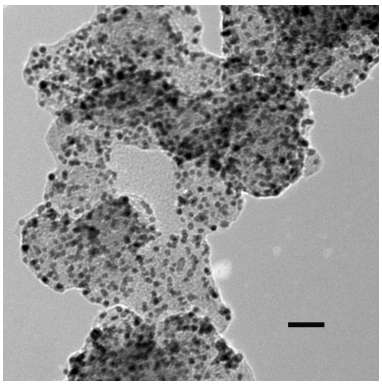

(a) Batch 1

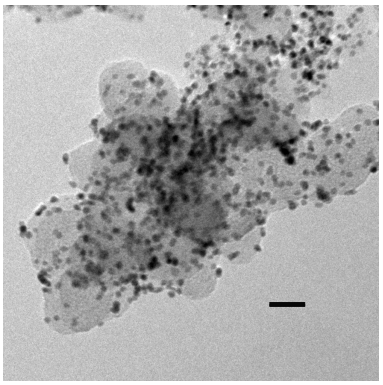

(b) Batch 2

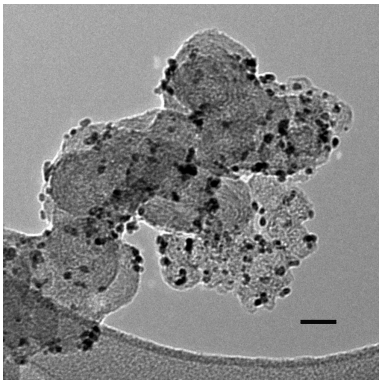

(c) Batch 3

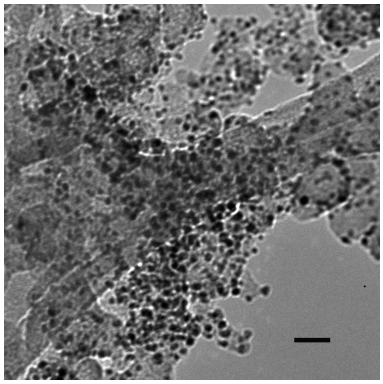

(d) Batch 4

Figure 2.4: Example of TEM images for the four batches synthesised at the laboratory. The scale bar is 20 nm in each image.

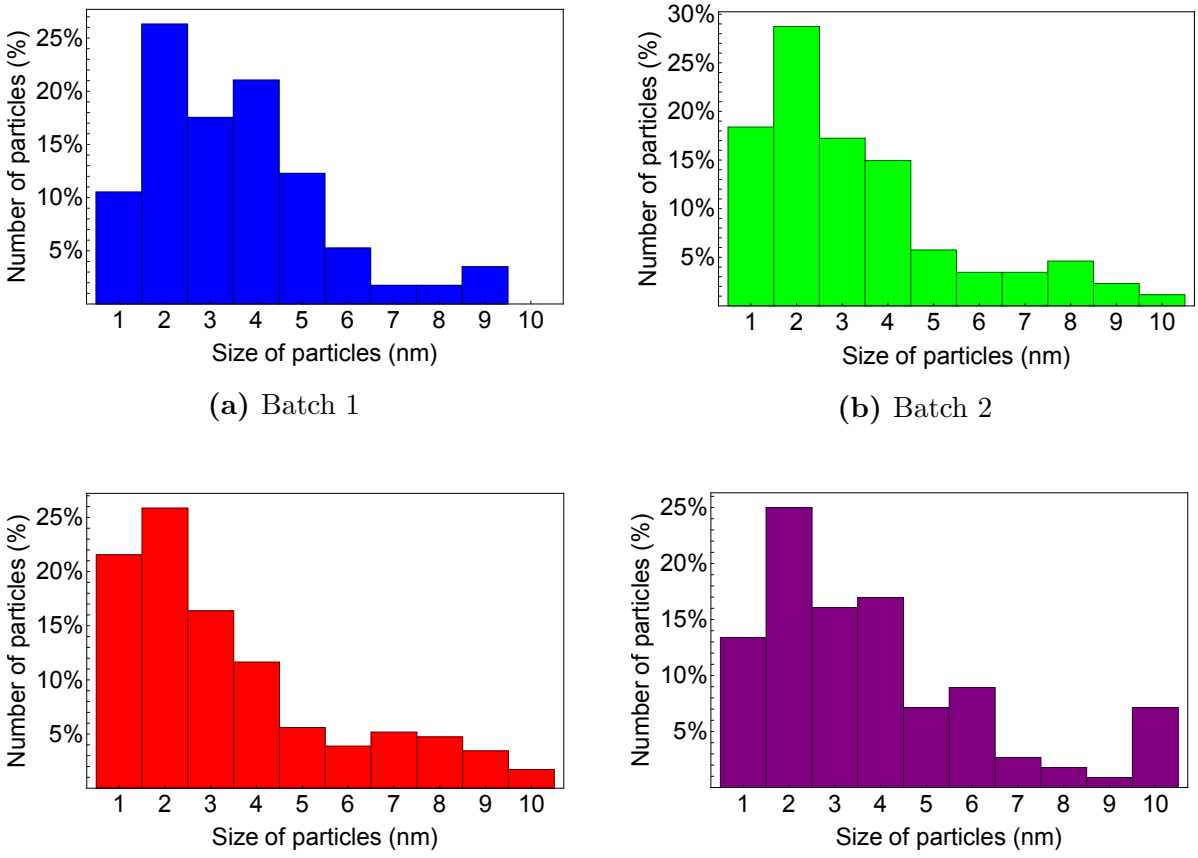

(a) Batch 1

(b) Batch 2

(c) Batch 3

(d) Batch 4

Figure 2.5: Histograms of the Pt particle size distribution obtained by TEM image analysis for the four batches.

The CO stripping voltammograms for the four batches synthesised at the laboratory and the commercial catalyst are shown in Fig. 2.6. The capacitive currents hint that the amount of electrocatalyst deposited on the WE is not the same for every batch. The commercial catalyst and the batch 1 have a similar capacitive signal near 0.4 V *vs.* NHE. As a result, the CO stripping peaks of batches 2, 3 and 4 cannot be used and compared to the others. The catalyst surface areas are thus computed using Eq. 2.3 for the batch 1 and the commercial catalyst.

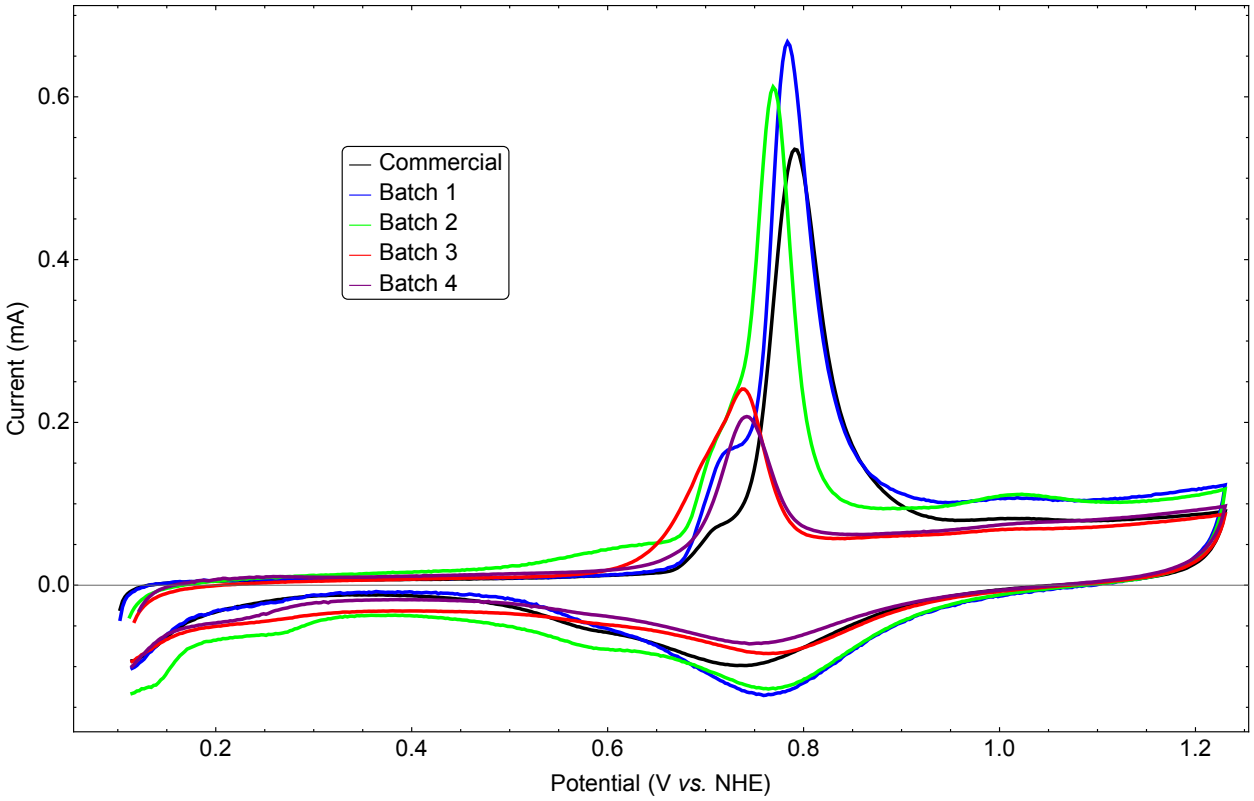

Figure 2.6: First cycle of the CO electrooxidation voltammograms for the four batches and the commercial catalyst. The scan speed is 20 mV s^{-1}. The CO stripping peak is located near 0.8 V *vs.* NHE.

For similar reasons, only the RDE experiments of the batch 1 and the commercial catalyst are displayed in Fig. 2.7a. The curves exhibit no current for a potential close to the standard potential of the oxygen reduction reaction ($\sim$ 1.0 V *vs.* NHE). The current then increases for smaller potential differences to finally reach the limiting mass transfer current i_l. For comparison, the RDE curves for different rotating speeds of the WE are shown in Fig. 2.7b. As expected, a larger rotating speed allows a better transport of the species to the Pt particles inside the electrolyte. The limiting current for $<$ 0.6 V *vs.* NHE is larger for 2500 rpm than for 1600 rpm.

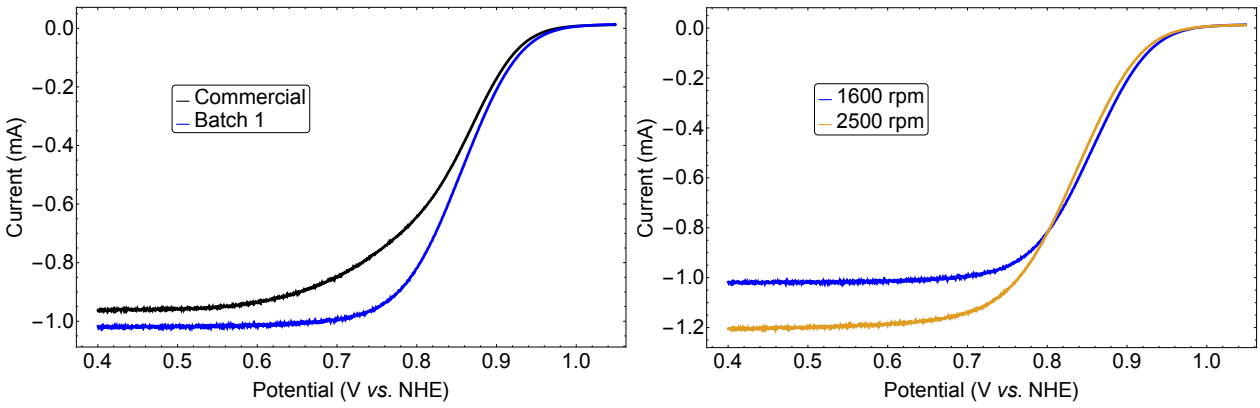

(a) **(b)**

Figure 2.7: Current-voltage curves for the positive scan (0.4 to 1.09 V *vs.* NHE) of the rotating disk electrode coated with (a) the batch 1 and the commercial catalyst for a WE rotating speed of 1600 rpm and (b) the batch 1 for WE rotating speeds of 1600 and 2500 rpm. The voltage scan speed is 2 mV s^{-1}.

The particle size values calculated with the different characterisation methods are reported in Table 2.1. The standard deviations of the distributions of the particle sizes obtained with the TEM are also displayed. Since the values obtained with the CO stripping are surface-sensitive, they in principle can be compared with the surface averaged diameter from the TEM [32]:

$$d_S = \frac{\Sigma n_i \, d_i^3}{\Sigma n_{id_i}^2} \tag{2.6}$$

and the volume-sensitive diameters obtained with XRD can be compared with the volume averaged diameter from the TEM [32]:

$$d_V = \frac{\Sigma n_i d_i^4}{\Sigma n_i d_i^3} \tag{2.7}$$

where n_i is the number of particles of size d_i. The activities are displayed in Table 2.2.

Table 2.1: Properties of the catalyst particles measured by physical and electrochemical techniques.

Catalyst	d_{TEM} (nm)	σ (nm)	d_S (nm)	d_V (nm)	d_{XRD} (nm)	$i_{c,i}/i_{c,com}$	S_{CO} (m^2 g^{-1})	d_{CO} (nm)
Batch 1	3.8	2.4	7.0	8.6	2.6	1.0	64.7	4.3
Batch 2	3.8	3.1	9.1	10.8	3.0	2.5	54.3	5.1
Batch 3	4.2	3.5	9.6	11.2	3.3	1.9	31.5	8.9
Batch 4	4.3	2.5	15.7	21.4	2.8	1.6	27.6	9.3
Commercial	/	/	/	/	2.1	1.0	80.5	3.5

d_{TEM}: Pt particle mean diameter, σ: standard deviation measured by TEM image analysis for the four batches. d_{XRD}: crystallite size for the four batches and the commercial catalyst. d_S: surface weighted particle size, d_V: volume weighted particle size obtained with TEM for the four catalyst batches. S_{CO}: Pt particle surface area, d_{CO}: particle diameter measured by CO stripping. $i_{c,i}/i_{c,com}$: normalised capacitive current.

Table 2.2: Kinetic current i_k, specific activity SA and mass activity MA for the synthesised and the commercial catalysts.

Catalyst	i_k (mA)	SA (A m_{Pt}^{-2})	MA (A g_{Pt}^{-1})
Batch 1	0.26	0.110	7.2
Commercial	0.21	0.087	5.7

The sizes of particles are displayed in Table 2.1 and the specific and mass activities are shown in Table 2.2. The XRD peak indicated that the electrocatalysts synthesised at the laboratory have small average crystallite sizes (2.6-3.3 nm) similar to the commercial powder (2.1 nm). This result is confirmed with the CO stripping peak of the batch 1 with a value of 4.3 nm for the particle size compared to 3.5 nm for the commercial catalyst. The RDE method displayed reasonable specific and mass activities for the batch 1 compared to the commercial catalyst and the catalysts prepared in a previous work at the laboratory [26]. The TEM image analysis led to particle size distributions with large standard deviations (Table 2.1). The image analysis showed much more inhomogeneity of the dispersion and agglomeration of the Pt particles than results obtained in the literature for a similar synthesis method [27, 26]. The surface weighted and volume weighted particle sizes from the TEM nevertheless dispayed large values indicating that a too low number of particle sizes was used for the computation. The data collection to get a larger amount of TEM micrographs was made impossible due to the health crisis. The values of the CO stripping for the batches 2 to

4 (Table 2.1) are far from the optimal size for the OR . The difference could come from the use of carbon xerogels instead of carbon black in the latter articles. The deposition of the catalyst is indeed sensitive to the textural and pore properties of the carbon support [33]. A more pragmatic reason for the agglomeration of the Pt particles could be the lack of control in the synthesis route concerning the addition of the Pt salt ($H_2PtCl_6.6H_2O$) in formic acid and carbon solution. A faster addition could lead to Pt agglomerates and thus to less dispersion. The injection flow of this compound should be carefully controlled for better results.

2.4 Conclusion

In this chapter, the synthesis of Pt catalyst was performed in view of further producing PEM fuel cells with variable catalytic compositions. Pt on carbon black was synthesised with the formic acid reduction technique. Four batches were made and characterised using the XRD, the TEM, the CO stripping technique and the RDE. While the activity of the catalyst was comparable to what is encountered in the literature, the sizes of the synthesised particles showed larger mean sizes and standard deviations. This inhomogeneity of Pt particle sizes could arise from a too fast injection of the Pt salt and thus a too fast reduction of Pt on the carbon support. In order to solve that problem, other syntheses were planned to be made with the use of a syringe pump to control the aforementioned injection. The experiments were unfortunately stopped due to the 2020 health crisis.

CHAPTER 3

PEM FUEL CELL MANUFACTURE AND CHARACTERISATION

3.1 Introduction

After the synthesis of the catalyst, PEM fuel cells can be manufactured and characterised. The hydrogen oxidation reaction at the anode and the oxygen reduction reaction at the cathode occur in the catalytic layers which are separated by the proton exchange membrane. Several techniques are listed in literature to make the catalytic layers. Among them, one can cite the electrodepostion, the sputter method [34] or wet techniques such as the doctor blade method [35] and the spray deposition [36]. With the latter, a mix of catalyst powder, Nafion® and solvents, called ink is first prepared. The ink is then sprayed in small droplets directly onto the PEM through a pressurised flow of air. The solvent is evaporated during the deposition as the PEM is placed on a heated substrate. The remaining dry deposit forms the catalytic layer.

The ink composition will define the final catalytic layer composition and, later, the performance of the fuel cell. The ratio between the weight of Nafion® and carbon (N/C) is of primary importance. A high concentration of Nafion® in the catalytic layer provides a good ionic conduction but can obstruct the carbon pores and the gas supply to the catalyst or can decrease the electric conductivity by isolating the carbon particles from each other. The N/C ratio is reported to be optimal between 0.3 and 0.8 [37, 13, 38].

A hot pressing is usually performed between the newly catalyst coated membrane and

the gas diffusion layers (GDLs). This provides better interfacial contact between the components and enhance the reproducibility [9]. This membrane-electrodes assembly is then clamped between the bipolar plates inside the cell.

After the manufacture and assembly process, a PEM fuel cell requires a break-in period in order to be fully activated and to reach its best performance [39]. The goal of manufacturers is to minimise this period of time in order to decrease the cost of an operating device and to consume less reactants. Even though no diagnostic tools were able to give the reasons for the necessity of an incubation step, hypotheses are listed in the literature [40]:

- the use of the catalyst allows to remove the impurities possibly introduced during the fabrication of the fuel cell;
- the activation step has beneficial effects on the structure of the catalytic layer and and leads to the formation of passages to catalyst particles that were previously inaccessible;
- the Nafion® included in the catalytic layer as well as the membrane have to be hydrated long enough to provide an acceptable ionic conduction.

Practitioners reported different procedures to accelerate the activation of the fuel cell as no standard procedure currently exists. Those methods include (i) exposing the fuel cell to higher gas pressure or temperature than the operating conditions [39, 41], (ii) restarting the fuel cell after stopping the gas supply and the heating system [42] or (iii) imposing a sequential profile of potentials [43].

In this master thesis, PEM fuel cells were made *via* techniques previously elaborated at the laboratory. The robot spray deposition method was used to deposit the catalyst onto the PEM [44] and the assembly was subsequently hot pressed. The catalyst utilised in this chapter was a commercial one as reproducibility is the main focus during the fabrication of the fuel cells. Indeed, the final aim of this project is to study the different limitations in the cathode catalytic layer by varying the composition in catalyst inside the PEM fuel cells. Making reproducible electrodes is key to be able to compare the different devices. Two sets of fuel cells with constant Pt loading on the width of the catalytic layer were fabricated in this chapter (EMEa, EMEb). The main difference in the manufacture is the diminution of the time duration of the robot spray for the second set (EMEb). The two sets of PEM fuel cells were then conditioned with different methods: the gas breaking (EMEa) and the sequential potential (EMEb). The conditioning processes were applied during three days to activate the PEM fuel cells. After each day, three characterisation techniques were used to evaluate their performance: impedance spectroscopy, *in situ* cyclic voltammetry and the

polarisation curve measurement.

3.2 Experimental

3.2.1 Manufacture and assembly process

Ink preparation

Two different inks were prepared to make the catalytic layer on either the anode or the cathode based on previous works made at the laboratory [44]. The catalyst powders used were 60 wt. % Pt on Vulcan XC72-R (Premetek P10A600) on the anode and 20 wt. % Pt on Vulcan XC72-R (Premetek P10A200) on the cathode. This difference was made for the purpose of studying the cathode voltage losses. To favor the reaction and to remove any overpotential on the anode side, a larger catalyst loading was used.

The N/C ratio was chosen as 0.8. The solvents were water and isopropyl alcohol. Their weight ratio was fixed at 1.3 to avoid the combustion of isopropyl alcohol. Indeed, in presence of air, the alcohol and then the carbon can ignite in contact with Pt, even at room temperature. Nafion® was added by incorporating Nafion® D2021 (20 wt. % Nafion®, 46 wt. % isopropanol, 34 wt. % water). The full composition of the inks was the following:

- 1.1 wt. % of C;
- 53.8 wt. % of MilliQ water;
- 4.9 wt. % of Nafion® D2021;
- 41.2 wt. % of isopropyl alcohol.

Note that this composition is given in term of C and not Pt/C. The amount of Pt/C catalyst has thus to be adapted to satisfy this composition depending on the Pt content. That means that the volume of Pt is neglected as Pt accounts for a negligible part of the ink volume. Indeed, the density of Pt is approximately 10 times the density of carbon.

The agitation procedures for the inks were determined by analysing the carbon particle sizes with the direct light scattering method. The agitation was considered to be sufficient when only one population of carbon particle sizes remained. The sizes were constant up to 1 h after the agitation process. The procedures are: (i) 40 min of ultrasonic probe for the 60 wt. % Pt/C and (ii) 15 min of sonic bath for the 20 wt. % Pt/C.

Robot spray deposition

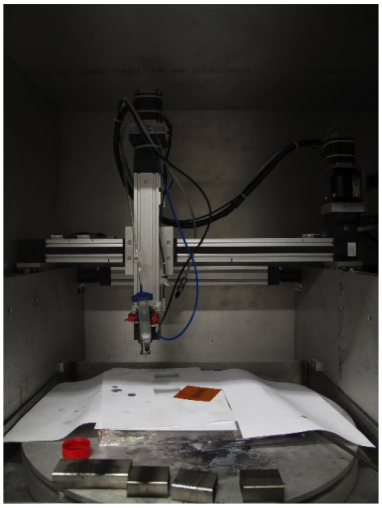

Figure 3.1: Photograph of the robot spray used in this project.

The spray deposition technique used in the scope of this project was performed with a nozzle connected to a robotic arm placed in a container (Fig. 3.1). A plate with controllable temperature was placed in the container of the robot spray in order to evaporate the solvents of the sprayed ink. A suction table linked to a pump with a porous mask made of glass fiber and PTFE was placed on the heated plate. The Nafion® membrane on which the catalytic layer was sprayed was put on a porous mask to avoid folding and to stay in position with respect to the spray travel. An aluminium mask with a square hole of 5 cm $\times$ 5 cm was on top of the set-up (Fig. 3.2). The size of the deposition (25 cm^2) was imposed by the cells and the test bench available at the laboratory. Air in pressurised bottles fed the nozzle of the spray and the outlet relative pressure was set at 0.4 MPa. The ink flow rate for the atomisation was controlled by a syringe pump.

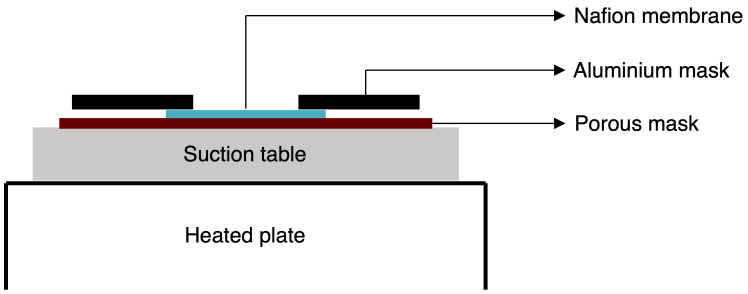

Figure 3.2: Schematic of the spray deposition set-up.

Two sets of catalytic layers on Nafion® membranes were sprayed, named EMEa and EMEb. The two sets of electrodes were prepared using slightly different spraying conditions (see below). The series EMEa was composed of 3 membrane-electrodes assemblies while the second series EMEb had 4. The proton exchange membranes were 8 cm × 8 cm squares of Nafion® 212. The operating procedure for the robot spray was similar to that described by Deschamps *et al.* [44]. The course imposed on each pass by the robotic spray consisted of 18 parallel lines of a length of 7 cm and a width of 2 mm between each step to form a 7 cm × 7 cm square (Fig. 3.3) at a speed equal to 15.1 cm s^{-1}. The nozzle was positioned at 33 mm in height. At this height, the deposit area covered by the nozzle is approximately 1 cm^2, and has a circular shape. A margin of 1 cm is necessary on each edge of the 5 cm × 5 cm coating to obtain a constant thickness over the whole sample surface, especially on the edges of the electrode. After each full pass on the sample, the spray moves away to a distance of 9 cm from the deposit (8 cm + the 1 cm margin) before going back to the initial position; this step is meant to prevent altering the edges of the layer at each pass. Indeed, the airflow itself tends to erode the layer over time. Some parameters were however different from those used by Deschamps *et al.* [44]: the temperature of the heated plate was fixed at 357 K (EMEa) and 367 K (EMEb) instead of 364 K and the flow rate was 0.3 mL min^{-1} (EMEa) and 0.45 mL min^{-1} (EMEb) instead of 0.72 mL min^{-1}. This increase of the temperature and the flow rate were performed in order to reduce the duration of the spray deposition and thus assess its effect on the reproducibility of the manufacturing process. The number of spray crossings was tuned with respect to the ink flow rate to to obtain a catalytic layer with a 10 μm thickness [44]. The Pt loading was approximately 0.13 mg cm^{-2} at the cathode and 0.81 mg cm^{-2} at the anode. The latter value is a high loading, especially for the hydrogen oxidation reaction [45]. This will ensure that no limitations may be ascribed to the anode side of the cell.

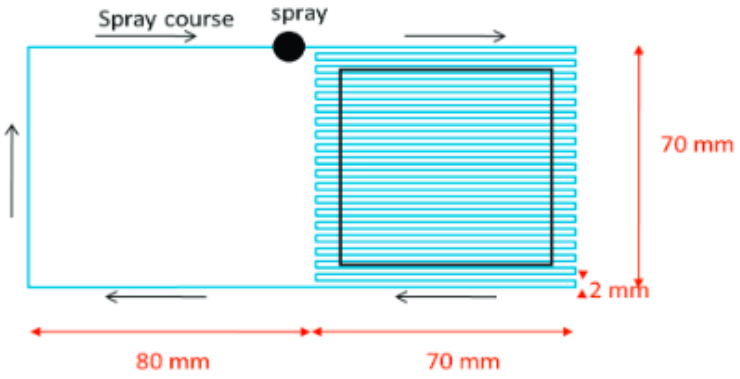

Figure 3.3: Schematic of the spray course followed by the nozzle during the robot spray deposition. [44]

Pressing and assembly

The catalyst coated membranes were then hot pressed with the 5.2 cm $\times$ 5.2 cm GDLs (Freudenberg H23C6, 250 μm) on each side to cover the entire deposit. To ensure the sealing of all the assembly, gaskets were disposed around the GDL, on the membrane where no catalyst was sprayed. The gaskets were first Silpad 400 (180 μm) for EMEa but after gas leakage during fuel cell tests, thicker t-Global L37-3F (250 μm) gaskets were used for the EMEb set of cells. The operating parameters of the hot pressing were a temperature of 403 K for 210 s with a force of 30 kN which are common values encountered in the literature [46, 47, 48].

It has to be noted that, with thicker gaskets (EMEb), the GDLs did not receive enough of the force applied by the hot pressing. As a result, the GDLs did not stick to the catalyst coated membrane. This made more difficult the last part of the process: the cell assembly. The cell (Fig. 3.5) is made of two bipolar plates, two current collectors and two flanges. The GDLs, gaskets and coated membrane were gingerly disposed between the bipolar plates (Fig. 3.4). The flanges were then clamped with the 8 screws using a torque wrench. The torque applied was 8 N m as a first step and was increased to 10 N m subsequently.

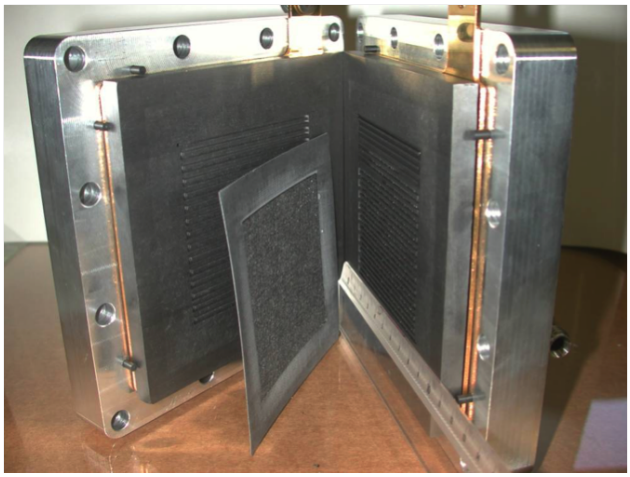

Figure 3.4: Photograph of the membrane-electrodes assembly inside the cell.

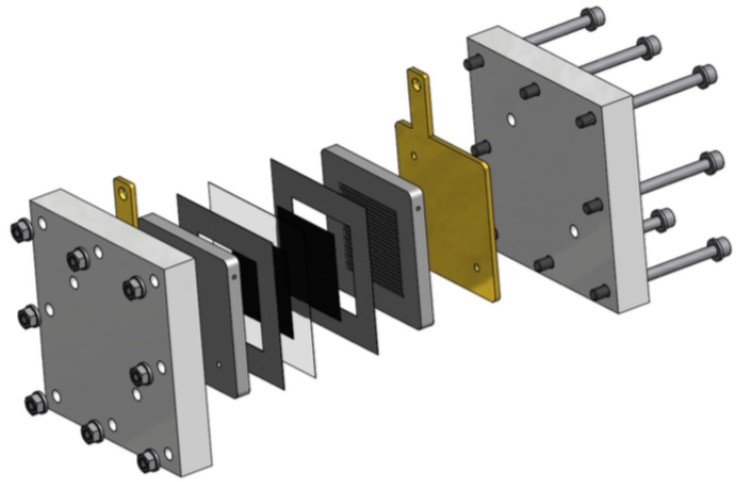

Figure 3.5: Schematic of the components of the cell.

3.2.2 Test bench description

(a)

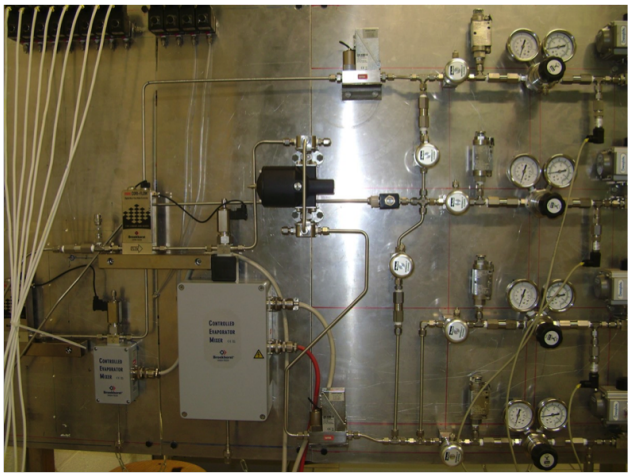

(b)

Figure 3.6: Photographs of (a) the potentiostat connected to the PEM fuel cell and (b) the gas lines that supply the device.

A schematic of the test bench used to characterise the PEM fuel cells is displayed in Fig. 3.7. Three gas lines are used for this project. The hydrogen and air gas lines feed the anode and the cathode, respectively. The nitrogen line can supply both sides of the fuel cell in order to purge the electrodes. The gases are delivered from pressurised bottles. The flow rates can be controlled through mass flow sensors before the inlets of the PEM fuel cell. The humidification system for the gases is made of a water flowmeter, a controlled evaporator

and mixing device allowing to tune the amount of evaporated water into the gas lines. As the saturated vapour pressure depends highly on the temperature, unwanted water condensation is prevented with the use of heating systems placed next to the humidifier and near the inlets and outlets of the fuel cell. The temperature of the cell itself is controlled *via* a thermocouple and two heating resistances located inside the bipolar plates. The pressure inside the gas lines are controlled after the fuel cell using backpressure sensors and I/P controllers. Finally, a potentiostat allows to control and record the potential and the current delivered by the fuel cell. The negative pole is connected to the anode to make it work as both the counter and reference electrode. This is made possible by the fact that the overpotential for the hydrogen oxidation reaction is very small and can be neglected. The anode potential is thus assumed constant and used as the reference. The cathode is plugged at the positive pole and is the working electrode.

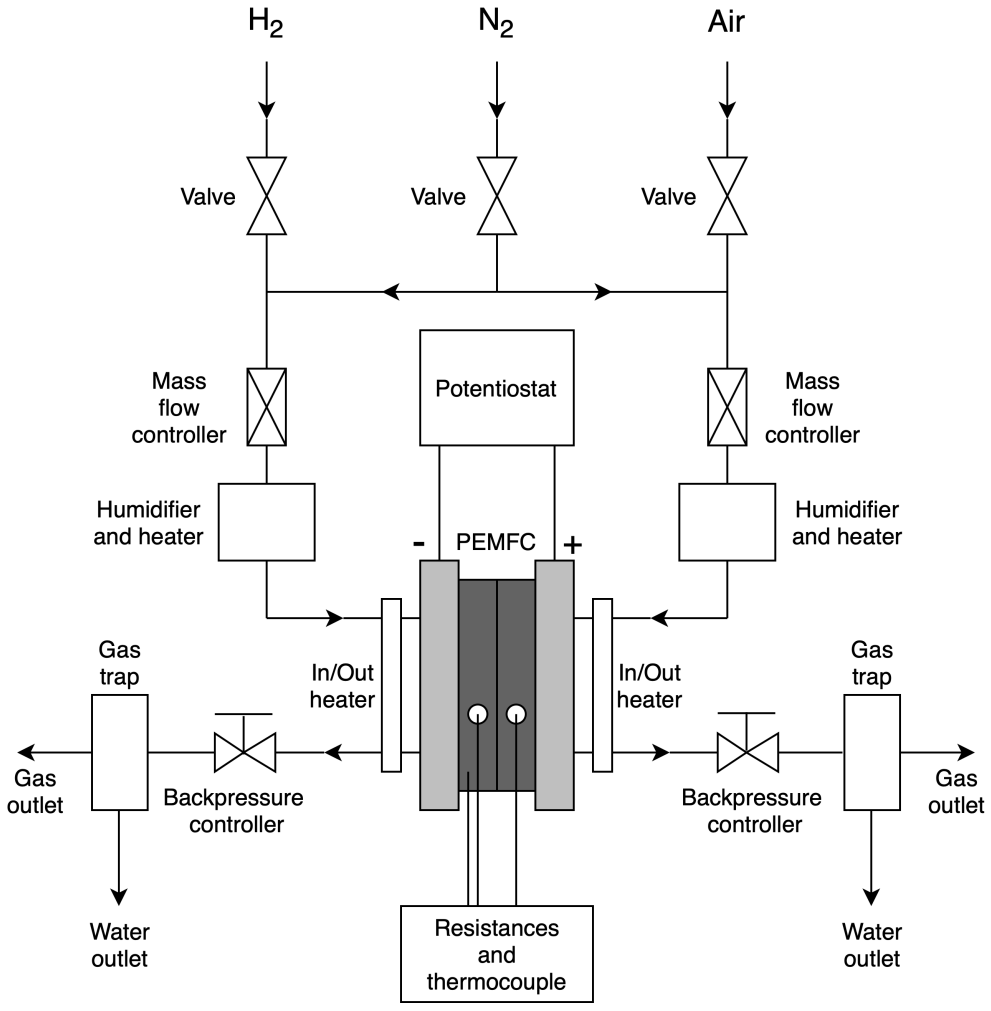

Figure 3.7: Schematic of the test bench used to characterise the fuel cells.

3.2.3 Operating conditions

The operating parameters used during the characterisation of the PEM fuel cells were chosen among the standard values encountered in the literature for similar Pt on carbon support catalysts [49, 50, 51, 52, 53]. The range of cell temperatures picked is 333 to 353 K, the gas pressure commonly applied on each electrode goes from 0 to 3 bar with respect to the atmospheric pressure and the typical relative humidity is 100 % in nearly all papers. A temperature higher than the ambient temperature increases the proton conductivity of Nafion® and the reaction kinetics, and high gas pressure decreases the mass transfer limitations at high current [54]. The flowrates were chosen in order for the PEM fuel cell to have a sufficient access to H_2/O_2 at high current. The calculation leading to the values of the operating flowrates is the following. The charge Q given by an electrochemical reaction is given by Faraday's law:

$$Q = n\,F\,N \tag{3.1}$$

where n is the number of electrons involved in the reaction, $F = 96485$ C mol^{-1} is the Faraday constant and N is the number of moles of the reactant [16]. Applying this equation to the case of the oxygen reduction reaction ($O_2 + 4\,e^- + 4\,H^+ \rightarrow 2\,H_2O$) and dividing by the time gives an expression involving the number of moles per unit of time of O_2 consumed $N_t(O_2)$:

$$I = 4\,F\,N_t(O_2) \tag{3.2}$$

with I being the current produced by the reaction. However, the fuel cells were fed with air and not directly with O_2. That is why the equation is expressed as a function of the flowrate of air, $d(\text{air})$. For convenience, the units chosen are mL min^{-1} and the equation becomes:

$$I = \frac{4\,F\,\chi(O_2)\,\rho(air)\,d(\text{air})}{60\,M(\text{air})} \tag{3.3}$$

with the fraction of O_2 in the air $\chi(O_2) = 0.2$ for the gas bottles used at the laboratory, the molar mass of air $M(air) = 28.97$ g mol^{-1} and the density of air $\rho(air) = 1.029\ 10^{-3}$ g mL^{-1} at 343 K and 0.5 bar with respect to the atmospheric pressure. In this configuration, the flowrate is the perfect amount of reactant per time unit delivered in order to get the desired current. In practice, due to the mass transport problems inside the electrodes of the PEM fuel cell, the flowrates were adapted so that the stoechiometry λ of reactants, *i.e.* the ratio between the supplied reactant and the appropriate amount of reactant, was higher than 1. This means that more reactant that the quantity needed to satisfy the reaction rate was supplied to the electrodes. The stoechiometry parameter is commonly higher for the cathode than the anode due to the slow kinetics of the reaction of the oxygen reduction reaction. The air flowrate at the cathode was thus fixed with the following expression:

$$d(\text{air}) = \frac{15\,M(\text{air})\,\lambda_c\,I_{max}}{F\,\chi(O_2)\,\rho(air)} \tag{3.4}$$

where λ_c is the stoechiometry of the gas supply at the cathode. Previous tests at the laboratory showed that the 25 cm^2 fuel cells could reach currents of the order of 25 A at 0.2 V. The stoechiometry was chosen as $\lambda_c = 1.8$, a value slightly smaller than those encountered in the literature [49, 52]. The air flowrate was thus equal to 1000 mL min^{-1} at 343 K and 0.5 bar with respect to the atmospheric pressure. A similar approach was used for the anode. The stoechiometry parameter was fixed at $\lambda_a = 1.2$ and the value of the flowrate at the anode was 400 mL min^{-1} at 343 K and 0.5 bar with respect to the atmospheric pressure. Table 3.1 summarises the chosen values of the operating parameters for this project.

Table 3.1: Operating conditions for the characterisation of the PEM fuel cells. The pressure and the relative humidity were fixed at the same values for both the anode and the cathode.

Parameter	Operating value
Temperature	343 K
Pressure	50 kPa
Relative humidity	100 %
Anode flow rate	400 mL min^{-1}
Cathode flow rate	1000 mL min^{-1}

3.2.4 Conditioning methods

In this project, the fuel cells of the first set (EMEa-1, EMEa-2, EMEa-3) were activated using a gas-braking technique. After stabilisation of the current at 0.6 V, the H_2 and air supplies were stopped and the anode and cathode were purged with N_2 for 5 min. In the meantime, the heating system was also stopped. Once the temperature had reached 303 K, the heating system and the gas supply were reactivated and the current was stabilised again at 0.6 V. This procedure was repeated at least twice a day during three days.

The second conditioning technique used to stabilise the second set of fuel cells (EMEb-1, EMEb-2, EMEb-3, EMEb-4) consisted in applying sequentially a potential from 0.1 V to 0.9 V and to 0.1 V again by 5-minute steps of 0.1 V (Fig. 3.8). This cycle was done at least twice a day during three days.

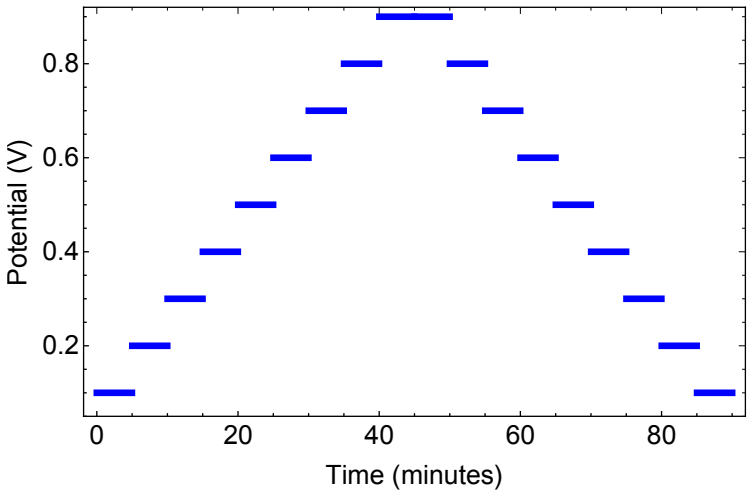

Figure 3.8: Potential applied during the conditioning process of the second set of fuel cells (EMEb-1, EMEb-2, EMEb-3, EMEb-4).

3.2.5 Characterisation

After each day of conditioning process, three characterisation techniques were used to measure the performance of the PEM fuel cells. The principle and procedure of those techniques are listed in this section. Apart from the conditioning method, it has to be recalled that the manufacture process of the two sets differed slightly. The flow rate for the spray of the catalytic layer was multiplied by 1.5, the temperature of the heated substrate in the spray was increased and thicker gaskets were used for the second set (EMEb) compared to the first one (EMEa).

Impedance spectroscopy

The impedance spectroscopy consists in modulating the voltage of the fuel cell by an AC voltage:

$$V(t) = V_0 \sin(\omega t) \tag{3.5}$$

where V_0 is its amplitude, ω is its angular frequency and t is the time within a range of known frequencies. The impedance of the system Z is then recorded based on the current response of the device for every frequency:

$$I = I_0 \sin(\omega t + \phi) \tag{3.6}$$

where I_0 and ϕ are the amplitude and the phase of the response. The impedance:

$$Z = \frac{V_0}{I_0} \exp(j \phi) \tag{3.7}$$

is reported on a Nyquist plot where its real and imaginary parts, Z_{re} and Z_{im} are plotted along the abscissa and ordinate, respectively. The amplitude of the AC voltage, V_0, is small ($\sim$ 10 mV) so that it does not affect the steady state of the cell [12].

When representing the Nyquist plot of a PEM fuel cell, two arcs are usually obtained. A common model used to explain the shape of the plot is the equivalent electrical circuit displayed in Fig. 3.9b [55]. The resistance R_{el} accounts for the internal resistance of the fuel cell, namely the PEM ionic resistance and the contact resistances in the whole device. The two other capacitors and resistances positioned in parallel are associated to the charge transfer and the mass transfer of the reactants. They are dissociated as both phenomena have a different relaxation time. A pure resistance does not provide any phase difference for the response of an AC signal. It only affects the Nyquist plot by shifting the plot through the right as it influences the real part of the impedance of the device. On the contrary, a resistance and a capacitor in parallel draw an arc on the plot as they together own a real and imaginary impedance.

In the scope of this characterisation process, the impedance spectroscopy is only used to get the internal resistance of the PEM fuel cells. The obtained value is an indication of the humidity of the proton exchange membrane as its conductivity depends highly on its water content [10]. The internal resistance also provides information about the contact resistance induced during the clamping of all the components at the end of the assembly of the cell [56].

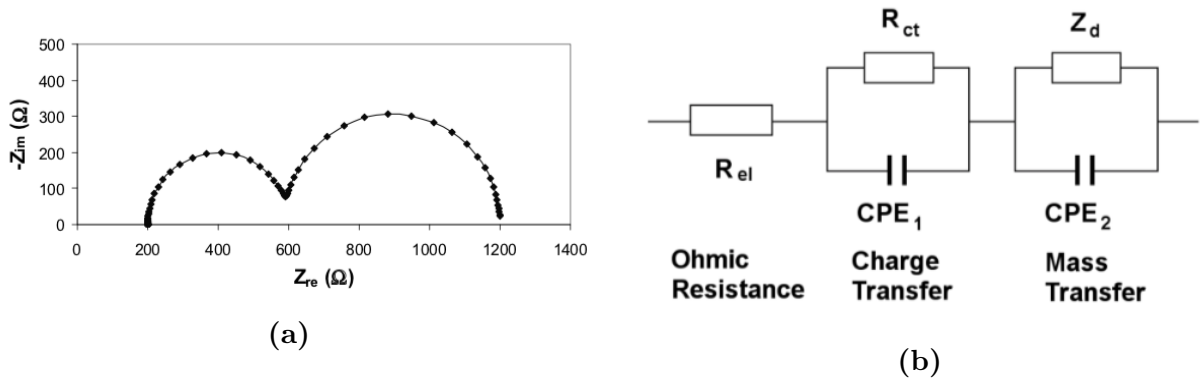

Figure 3.9: Nyquist plot (a) and PEM fuel equivalent cell circuit model (b). [55]

The chosen steady state voltage that is modulated is 0.6 V in this project. This value is a common working voltage as the PEM fuel cell delivers a high power at that potential. The range of frequencies scanned to get the Nyquist plot was 150 mHz to 20 kHz.

In situ cyclic voltammetry

This characterisation technique is used to measure the catalyst surface area available of the cathode catalyst layer in the PEM fuel cell. This experiment requires different conditions than the operating conditions regarding the gas supply (Table 3.1). The experimental procedure is the following.

- At open circuit voltage, while H_2 is still supplied to the anode (300 mL min^{-1}), N_2 purges the cathode (800 mL min^{-1}) from any residual O_2 until the value of the open circuit voltage E_{OCV} is stabilised.
- The flowrates of H_2 and N_2 are fixed at 100 and 300 mL min^{-1}, respectively.
- Once E_{OCV} is again stabilised, a linear slope of potential is applied to the fuel cell from 0.05 to 1.2 V and again to 0.05 V with a scan speed of 20 mV s^{-1}. The current is recorded and plotted as a function of the potential.

Purging the cathode from O_2 allows to access to the current associated to the catalyst surface state at the cathode which is usually masked by the oxygen reduction current. At low potential ($E = 0.05 - 0.3$ V), the Pt particles adsorb H on their surface and release it as the potential of the cathode increases [12]:

$$Pt - H_{ads} \rightarrow Pt + H^+ + e^-. \tag{3.8}$$

This reaction produces electrons and thus a current. The current-potential curve includes a peak from 0.05 V to approximately 0.3 V in the positive scan. Similarly, during the negative scan, the inverse reaction occurs and electrons are captured for H to be adsorbed at the Pt surface. When reaching values of the cathode potential of 0.3 to 0.5 V, the Pt particles undergo no modification of their surface. The difference in current in this region is only caused by the charge and discharge of the carbon and ionomer contained in the catalyst layer. This capacitive effect is in fact present in the whole range of potential. For $E = 0.6 - 1.2V$, the Pt surface is oxidised to form $Pt - O - H$, $Pt - (O - H)_2$ or $Pt - O$ [12]. These processes release one or two electrons during the positive voltage scan and capture them during the negative scan. Once again, these reactions are responsible for peaks in the current-voltage curve.

What can be concluded from the aforementioned electrochemical reactions is that a clear relation exists between the number of active sites in the whole catalytic layer and the electrons produced to form a peak. From that observation, the electrochemical Pt surface area $EPSA$ (m^2 g_{Pt}^{-1}) can be retrieved [30]:

$$EPSA = \frac{S_{peak}}{v_{scan}\, m_{Pt}\, C_H} \tag{3.9}$$

where S_{peak} (mA V) is the surface of the peak of the desorption of H during the positive scan ($E = 0.05 - 0.3$ V), v_{scan} (V s^{-1}) is the scan rate used during the experiment, m_{Pt} (g) is the Pt mass of the cathode electrode and $C_H = 0.21$ mC cm^{-2} is the charge required to desorb a monolayer of H from a Pt surface. This value of the $EPSA$ differs from the S_{CO} measured with the rotating disk electrode setup in Chapter 2. In the RDE configuration, the electrolyte is liquid and it is assumed that it reaches the entire available Pt surface of the electrode. In the case of the cyclic voltammetry in the PEM fuel cell, the Pt particles are participating to the reaction depending on the Nafion® distribution in the catalytic layers. Indeed, only the particles reaching the triple contact (Pt/Nafion®/Carbon) are electrochemically active.

A final remark can be made on the value of the current displayed on the obtained voltammogram: the curve is not centered on 0 A. The shifting current is associated to the H_2 crossover. As explained in the Chapter 1, the membrane can be permeable to some H_2 molecules and let those pass to the cathode. The hydrogen is then oxidised and electrons are released at the cathode. A constant current on the whole range of the scanned potential is therefore detected besides the current associated to the Pt surface.

Polarisation curve

The last characterisation technique is the record of the fuel cell performance through the polarisation curve. This curve was obtained by plotting the current from the open circuit voltage to a voltage close to 0 V. The procedure used here consisted in stabilising the cell at open circuit voltage for 10 s and then recording the polarisation curve with a scan speed of 50 mV s^{-1}. This high value of scan speed was used in order to reduce the effect of the accumulation of produced water in the catalytic layer that may block the gas supply and alter the performance of the fuel cell [14].

As explained in section 1.4, three kinds of overpotentials are commonly distinguished in a PEM fuel cell. Each of these voltage losses have a potential region where they are significant. Near the open circuit voltage E_{OCV}, the kinetic overpotential is dominant and increases until being nearly constant. When power is produced by the fuel cell, the current decreases linearly with the cell voltage due to the ohmic overpotential. Moreover, from 0.4 V to 0 V, the diffusion overpotential hinders the current to be further increased. Knowing this, the currents obtained at 0.85, 0.6 and 0.3 V are compared between the fuel cells of both sets. The standard deviation in current is then used as the limit of reproducibility of the set.

3.3 Results and discussion

For the sake of example, the high frequency Nyquist plots for EMEa-3 and EMEb-3 are reported in Fig. 3.10. The values of the high frequency resistance of the two sets of PEM fuel cells are reported in Table 3.2.

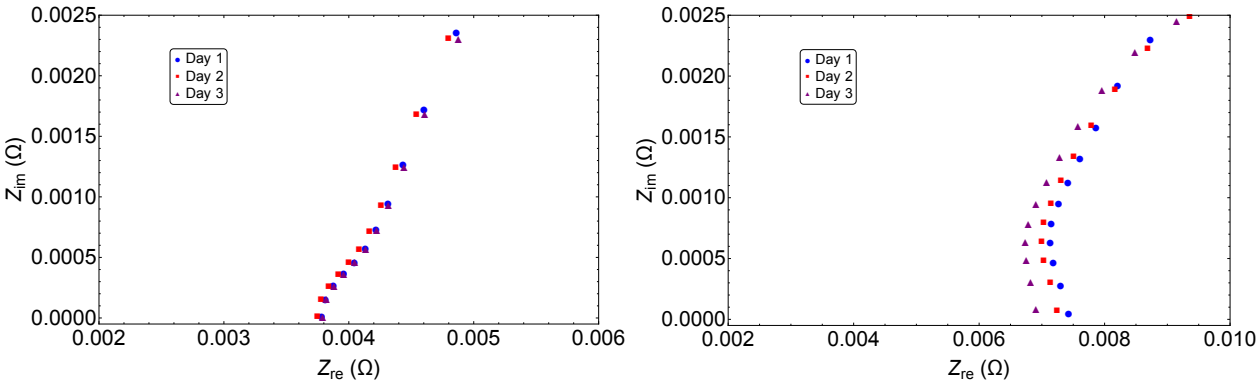

(a) EMEa-3 **(b)** EMEb-3

Figure 3.10: Examples of Nyquist plots at high frequencies used to retrieve the internal resistance of the PEM fuel cells.

Table 3.2: High frequency resistances along the conditioning processes for the two sets of fuel cells.

	R_{el} at day 1 (mΩ)	R_{el} at day 2 (mΩ)	R_{el} at day 3 (mΩ)
EMEa-1	3.8	3.6	3.6
EMEa-2	3.9	3.9	3.9
EMEa-3	3.9	3.9	3.8
EMEb-1	9.4	8.8	9.3
EMEb-2	7.0	6.7	6.4
EMEb-3	7.6	7.4	7.0
EMEb-4	6.7	6.3	5.5

Every fuel cell of the two sets exhibits the same typical shape for current-potential curve described previously regardless of the progress of the activation of the cell. The voltammogram of EMEb-1 is displayed in Fig. 3.11. The *EPSA* values are reported in Table

3.3. The experiment was conducted only once or twice during the conditioning process for EMEa. Considering the clear dependency of the $EPSA$ values on the day of conditioning with EMEa, the experiment was repeated each day for the second set (EMEb).

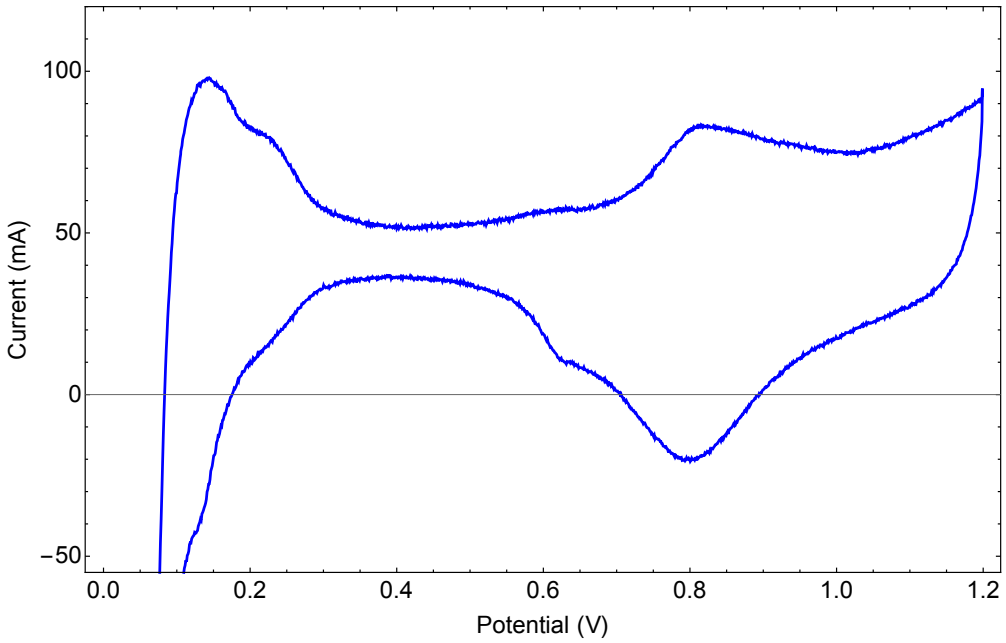

Figure 3.11: Current-potential curve for the *in situ* cyclic voltammetry of EMEb-1 at day 3.

Table 3.3: $EPSA$ for the two sets of fuel cells along the three days of conditioning process.

	$EPSA$ at day 1 ($m^2\ g_{Pt}^{-1}$)	$EPSA$ at day 2 ($m^2\ g_{Pt}^{-1}$)	$EPSA$ at day 3 ($m^2\ g_{Pt}^{-1}$)
EMEa-1	/	47.5	/
EMEa-2	/	47.0	40.4
EMEa-3	/	/	39.0
EMEb-1	48.1	46.0	43.1
EMEb-2	46.5	43.7	43.0
EMEb-3	47.9	44.9	41.2
EMEb-4	46.6	43.9	41.9

The currents at cell potential of 0.85, 0.6 and 0.3 V obtained on the polarisation curve are reported in Fig. 3.12 and 3.13 for three days of conditioning. The final performance reached by the fuel cells are displayed in Fig. 3.14 and 3.15 *via* the polarisation curves at day 3 of conditioning. The mean values and standard deviations for the final currents at 0.6

and 0.3 V are shown in Table 3.4.

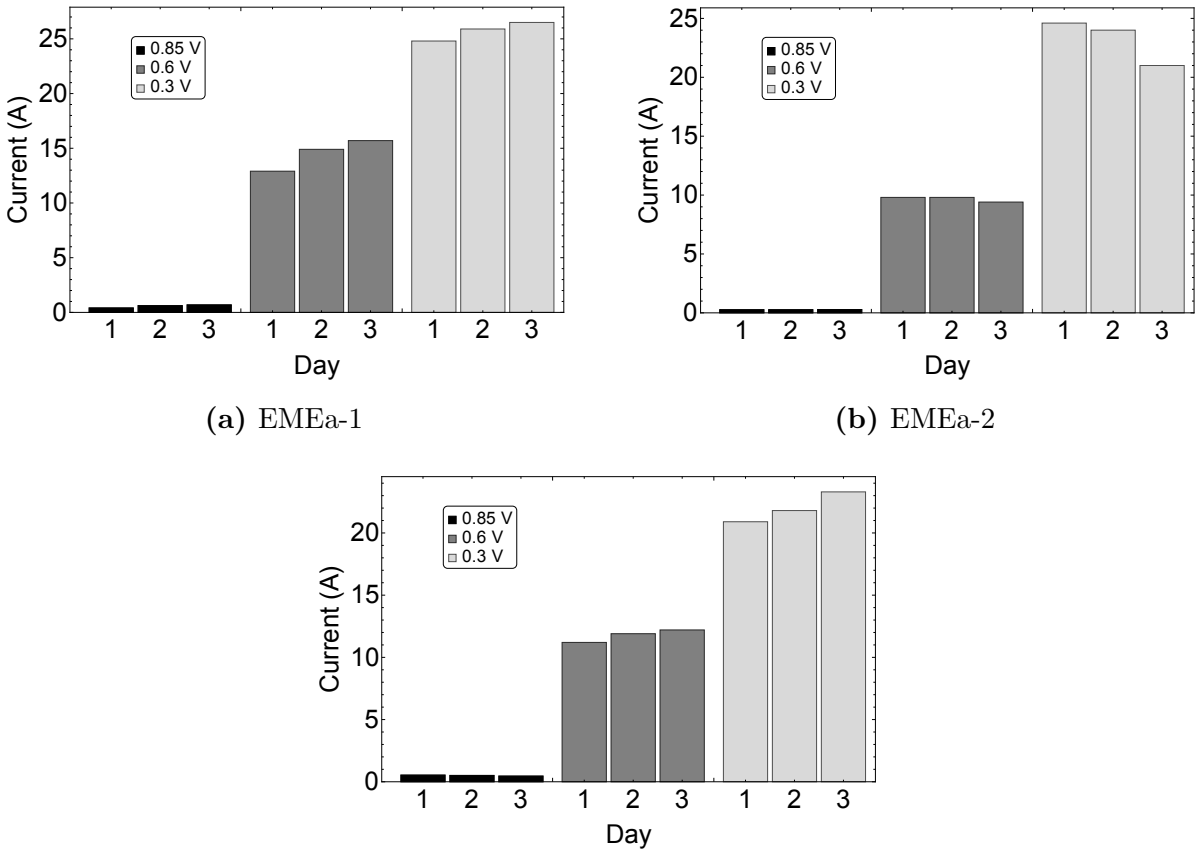

(a) EMEa-1

(b) EMEa-2

(c) EMEa-3

Figure 3.12: Currents obtained on the polarisation curves at 0.85, 0.6 and 0.3 V during the conditioning process for the first set of fuel cells (EMEa).

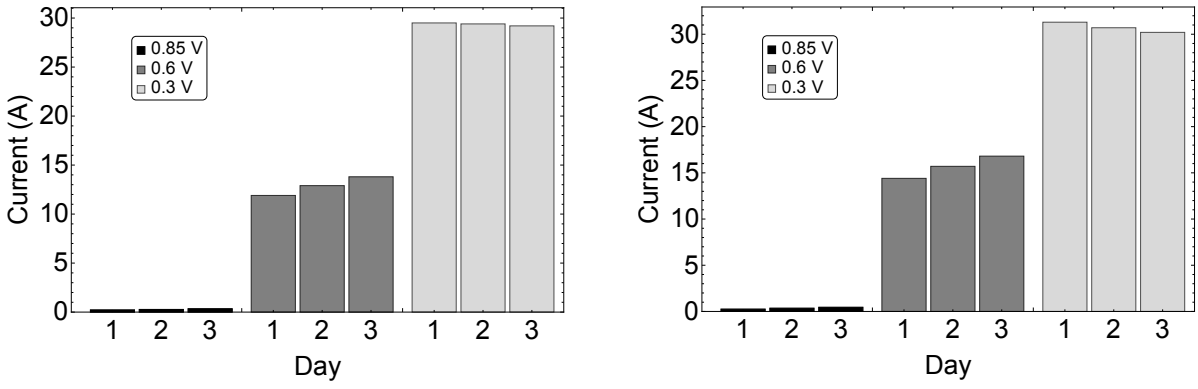

(a) EMEb-1

(b) EMEb-2

(c) EMEb-3

(d) EMEb-4

Figure 3.13: Currents obtained on the polarisation curves at 0.85, 0.6 and 0.3 V during the conditioning process for the second set of fuel cells (EMEb).

Conditioning

The values of the high frequency resistances are nearly constant (Table 3.2) and their slight difference could not explain a modification of the performance observed on the polarisation curves (Fig. 3.12 and 3.13). The impedance spectroscopy showed a nearly constant ohmic resistance for every device (Table 3.2). This indicates that the membrane hydration is nearly immediate thanks to the humidification of the gas supplies. Therefore, the conditioning process do not seem to influence the high frequency resistance.

The available catalyst surface area computed with the *in situ* cyclic voltammetry shows a clear dependence on the day of conditioning (Table 3.3). The $EPSA$ drops of at least 10 % from day 1 to day 3 for the second set (EMEb). This could be caused by the degradation of the Pt catalyst. Two mechanisms are listed in the literature to explain this result: the migration of Pt to form agglomerates with smaller surface area per weight of catalyst and the dissolution of the catalyst when it is in its oxidised form [57]. This degradation could be inherent to the commercial catalyst employed here (20 wt. % Pt/C from Premetek) and could be part of the stabilisation process.

Nevertheless, the polarisation curve near the open circuit voltage (0.85 V), where the activity of the catalytic layer is the most important parameter, increases in performance each day for every fuel cell (Fig. 3.12 and 3.13). Regarding the rest of the polarisation curve, the gas-braking technique seems to completely activate the performance of the first set of fuel cells at 0.6 V after the three days although smaller time of conditioning is reported for a similar activation procedure [40]. However, the performance at 0.3 V is reduced throughout the process for EMEa-2 and increases for the two other cells (EMEa-1, EMEa-3). The second conditioning technique involving sequential potentials could fully activate EMEb-1 and EMEb-2 at 0.3 V after one day but the performance at 0.6 V never reaches a plateau during the whole process. On the contrary, EMEb-3 and EMEb-4 seemed stable at 0.6 V after the first day but their performance declined with time at 0.3 V. As the two conditioning methods did not successfully activate the fuel cells, other techniques should be envisaged. A method involving higher pressure for the gas reactants was reported as efficient [39, 41] and could be used for further works.

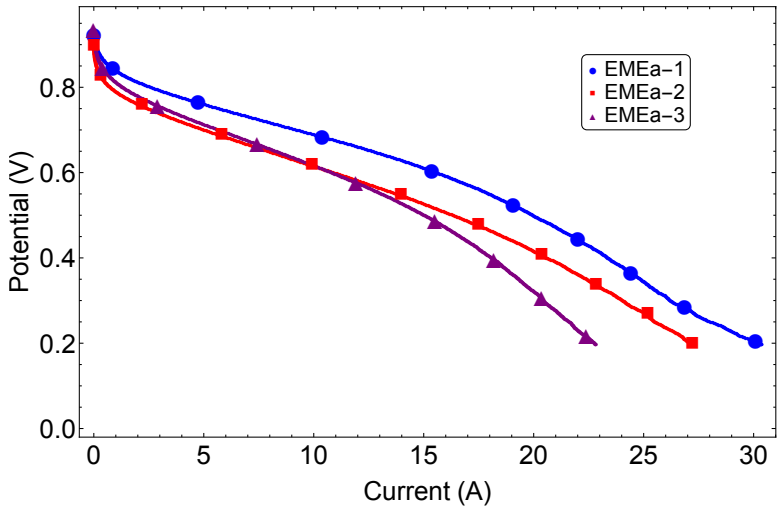

Figure 3.14: Polarisation curves for the first set of fuel cells (EMEa) at day 3.

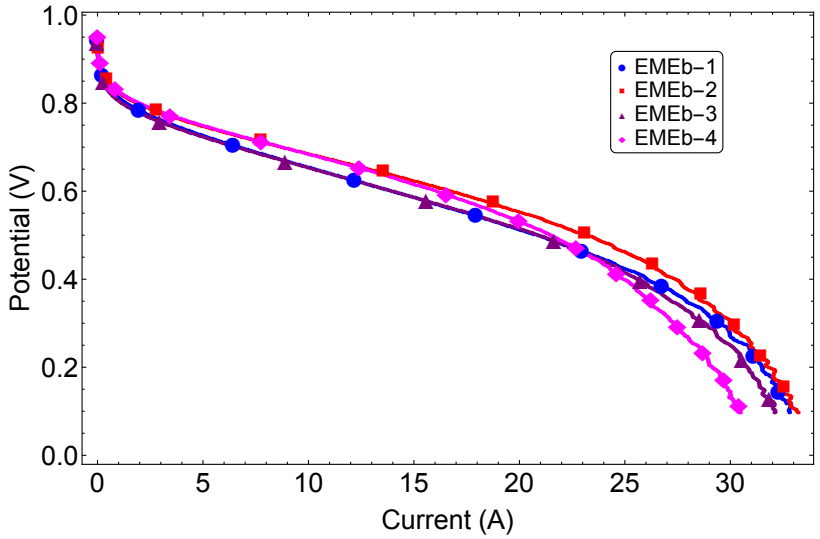

Figure 3.15: Polarisation curves for the second set of fuel cells (EMEb) at day 3.

Table 3.4: Mean value $\bar{i}$ and standard deviation σ_i for the currents at 0.6 and 0.3 V obtained at day 3 with the two sets of fuel cells manufactured and characterised at the laboratory. The standard deviation divided by the mean value gives the standard deviation in %.

	$\bar{i}$ at 0.6 V (A)	σ_i at 0.6 V (A)	σ_i at 0.6 V (%)
EMEa	12.4	2.3	18.5
EMEb	14.9	1.4	9.4
	$\bar{i}$ at 0.3 V (A)	σ_i at 0.3 V (A)	σ_i at 0.3 V (%)
EMEa	23.6	2.8	11.8
EMEb	28.3	2.1	7.4

Reproducibility

The fuel cells of the first set have similar ohmic resistances given by impedance spectroscopy (Table 3.2). This homogeneity is not retrieved with the second set. The thicker gaskets used for EMEb could be the reason for larger values and differences for R_{el}. Indeed, the latter gaskets could have undergone more of the force applied by the hot pressing during the manufacture process due to their larger thickness. As a result, the contact obtained between the membrane/catalytic layer and the GDL would be less enhanced than EMEa with the thinner gaskets.

The performance obtained with the polarisation curves at day 3 for the first set showed a relatively poor reproducibility (Table 3.4). The ratio between standard deviation and mean value of the current at 0.6 V is 18.5 %. This value is nearly divided by two for the second set of fuel cells. This excellent degree of reproducibility was made possible by the control given by the spray technique and more precisely, could originate from the increase of the flow rate during the spray of the catalytic layer on the PEM. Indeed, the operating parameters of the spray, such as temperature [58] are known to impact widely the porosity of the catalytic layer. As both air and water are sputtered during the spray, the temperature and humidity in the container of the robot spray is not constant. Lowering the duration of the spray would result in a smaller change of the temperature and the humidity. The impact of the variation of the operating conditions during the fabrication process is thus reduced with a larger flow rate of the spray.

3.4 Conclusion

The aim of this chapter was to manufacture reproducible membrane-electrodes assemblies in order to be able to characterise and discriminate PEM fuel cells with different catalyst compositions. The robot spray deposition technique previously elaborated at the laboratory was used to deposit the catalytic layer on the PEM. Two sets of PEM fuel cells (EMEa and EMEb) with constant catalytic composition were manufactured and characterised. After the cell assembly, both sets were conditioned using a different method. EMEa was activated using a gas breaking technique while the conditioning method for EMEb consisted in applying a sequential potential to the cells. Unfortunately, none of those methods were able to satisfactorily activate the fuel cells. The final performance of both sets showed that the reproducibility of the second series (EMEb) was increased with respect to the first one (EMEa). The increase of the flow rate of the spray during the deposit of the catalytic layer on the PEM is suspected to be primary factor behind this reproducibility rise.

While the search for an even more reproducible manufacture process could have been carried on, the logic continuation of that chapter would have been to manufacture and characterise PEM fuel cells with different catalytic compositions as explained in the introduction. However, the 2020 health crisis did not allow to continue the experimental work. The next chapter is thus dedicated to the numerical modelling of the cathode catalytic layer which we are interested in. This model will be in any case useful to analyse the experimental results obtained with different catalytic layer architectures.

CHAPTER 4

CATHODE CATALYTIC LAYER MODEL

4.1 Introduction

During the oxygen reduction reaction, the reactants have to travel inside the complex structure of the catalytic layer to reach an active site. For the reaction to occur close to the gas diffusion layer, at the oxygen inlet, the protons have to be conducted in the Nafion® network built in the carbon pores. Similarly, the electrons have to be conducted and the oxygen has to diffuse and to cross the whole catalytic layer to react on a catalyst particle close to the PEM. Those configurations lead to different voltage losses that cannot be retrieved by a single polarisation curve.

The last part of this project aims at the study of those voltage losses inside the PEM fuel cell through the modelling of the cathode catalytic layer. Inside the PEM fuel cell, several physicochemical phenomena are involved such as chemical reactions, gas diffusion or electric and proton conduction. Due to the non linearity of the equation linking the overpotential and the production of current (see Eq. 1.20), the elaboration of a model requires a numerical strategy. Indeed, no analytical solution predicts the performance or the behaviour of the reactants in the PEM fuel cell.

A 1D pseudo-homogeneous model similar to You and Liu [59] is developed in this chapter. This model will provide a basis for the understanding of the behaviour of the compounds involved in the oxygen reduction reaction. The aim is to analyse the dependency of the reaction rate with the position in the catalytic layer while varying the physical constants of the catalytic layer. Finally, the impact of the mass transport parameters on the polarization

curve, *i.e.* on the voltage loss as the current increases, is analysed.

4.2 Mathematical description

The modelling of the PEM fuel cell is restricted to the cathode catalytic layer of the PEM fuel cell. It does not deal with the anode reaction side and the voltage loss at the anode is thus neglected. The oxygen reduction reaction exhibits a small exchange current [18] and consequently a slow kinetics compared to the hydrogen oxidation reaction. Also, the diffusion of the hydrogen at the anode is faster than the diffusion of oxygen in the air at the cathode. The slow kinetics coupled with the slow diffusion justifies to restrict the analysis to the cathode side of the PEM fuel cell. The ohmic resistance related to the Nafion® membrane and the contacts between the components of the device are also set aside in this model.

The catalytic layer is a composite material made of a porous carbon support, onto which the catalyst particles are dispersed, and Nafion® as a proton conductor. Oxygen is supplied to the catalyst sites through the complex network of pores of the layer. The present model assumes an homogeneous catalytic layer with a constant diffusion coefficient and with uniform thickness. The propagation of the species (protons, electrons and oxygen) is limited to the longitudinal direction (Fig. 4.1) and the effect of the side boundaries of the catalytic layer is not taken into account.

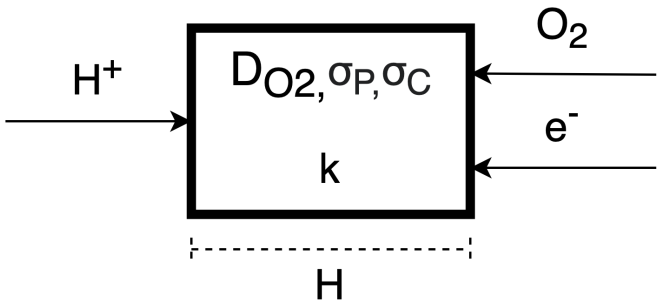

Figure 4.1: Schematic of the pseudo-homogeneous cathodic catalytic layer modeled in this chapter. D_{O2}, σ_P and σ_C are the diffusion coefficient, the ionic and electrical conductivity. k is the reaction rate constant. H is the catalytic layer thickness.

In this model, three transport parameters are introduced: D_{O2}, σ_P and σ_C. These correspond to the diffusion of oxygen, the proton conductivity in the Nafion® and the electric conductivity in the carbon support, respectively. The reactivity of the catalytic layer is

described using the reaction rate constant k. In the next subsections, the different transport phenomena and the reaction rate will be developed in order to retrieve the equations that describe the model.

4.2.1 Potentials and reaction rate

The kinetic overpotential or kinetic voltage loss η_k inside the cathode catalytic layer of the PEM fuel cell is given by [3]:

$$\eta_k(z) = V_C(z) - V_P(z) - E_{Nernst} \tag{4.1}$$

where V_C is the potential of the electrons inside the carbon, V_P is the potential of the protons inside the Nafion®, E_{Nernst} is the Nernst potential for the oxygen reduction reaction (ORR) and z is the coordinate accounting for the catalytic layer depth. This equation means that the kinetic loss is related to the difference in potential between the electrons and the protons when the chemical reaction happens and that it depends on the position of the active site in the catalytic layer.

From transition state theory [16], one can derive the reaction rate R of a redox reaction:

$$\mathrm{Ox} + \mathrm{n\,e^-} \underset{\text{backward}}{\overset{\text{forward}}{\rightleftharpoons}} \mathrm{Red} \tag{4.2}$$

at one electrode:

$$R = R_f - R_b = \left(k_f\, C_{ox}\, \exp\left[-\frac{\alpha\, F\, (E - E_0)}{R\, T} \right] - k_b\, C_{red}\, \exp\left[\frac{(1-\alpha)\, F\, (E - E_0)}{R\, T} \right] \right) \tag{4.3}$$

where R_f and R_b are the forward (reduction) and backward (oxidation) reactions rates, C_{ox} and C_{red} are the concentrations in oxidant and reductant at the electrode, E is the potential of the electrode, E_0 is the standard potential of the reaction and k_f and k_b are the reaction rate constants. At equilibrium (Nernst potential), one has:

$$R_f = R_b \tag{4.4}$$

$$k_f\, C_{ox}^0\, \exp\left[-\frac{\alpha\, F\, (E_{Nernst} - E_0)}{R\, T} \right] = k_b\, C_{red}^0\, \exp\left[\frac{(1-\alpha)\, F\, (E_{Nernst} - E_0)}{R\, T} \right] = k\, C_{ox}^0 \tag{4.5}$$

with C_{ox}^0 and C_{red}^0 the constant bulk concentrations in oxidant and reductant. Indeed, if the electrode is at equilibrium, no net consuption of reactant is observed and no concentration gradient exist between the electrode surface and the bulk fluid. According to Eq. 4.3 and 4.5, the reaction rate becomes

$$R = k\, C_{ox}^0 \left(\frac{C_{ox}}{C_{ox}^0}\, \exp\left[-\frac{\alpha\, F\, (E - E_{Nernst})}{R\, T} \right] - \frac{C_{red}}{C_{red}^0}\, \exp\left[\frac{(1-\alpha)\, F\, (E - E_{Nernst})}{R\, T} \right] \right). \tag{4.6}$$

By applying this relation to the cathode electrode of the PEM fuel cell, one gets:

$$R = k\, C_{O2}^{0} \left(\frac{C_{O2}}{C_{O2}^{0}} \exp\left[-\frac{\alpha\, F\, \eta_k}{R\, T} \right] - \frac{C_{H2O}}{C_{H2O}^{0}} \exp\left[\frac{(1-\alpha)\, F\, \eta_k}{R\, T} \right] \right). \tag{4.7}$$

Assuming that the water content at the cathode is not a limiting parameter of the backward reaction for the operating conditions of the fuel cell:

$$\frac{C_{H2O}}{C_{H2O}^{0}} = 1 \tag{4.8}$$

and the reaction rate can then be written as:

$$R(z) = k\, C_{O2}^{0} \left(\frac{C_{O2}(z)}{C_{O2}^{0}} \exp\left[-\frac{\alpha\ F\, \eta_k(z)}{R\, T} \right] - \exp\left[\frac{(1-\alpha)\ F\, \eta_k(z)}{R\, T} \right] \right) \tag{4.9}$$

with a positive reaction rate for the ORR as $\eta_k < 0$ for operating conditions of the PEM fuel cell. The constant k is related to the catalyst surface area in the catalytic layer. α is the transfer cefficient for the ORR, considered equal to 0.5, meaning that the current *vs.* voltage curves of both oxidation and reduction are symmetric. R is the the gas constant, F is the Faraday constant and T is the temperature at the electrode, considered constant on the entire catalytic layer. C_{O2} and C_{O2}^{0} are the concentrations of O_2 at the catalyst and at the inlet of the catalytic layer. It has to be noted that these relations are defined for redox reactions with one electron exchanged. The parameter n_α is often introduced in the exponential factors for multi steps and multi electrons exchange reactions (see Chapter 1). However, its value for ORR has been mainly reported as equal to 1 [18] at high current density and n_α is omitted here.

The ORR Nernst equation written in term of the concentrations of the reactants:

$$E_{Nernst}(z) = E_{0,c} + \frac{RT}{4F} \ln\left[\frac{C_{O2}(z)}{C_{O2}^{0}} \right] \tag{4.10}$$

can be incorporated in the kinetic overpotential $\eta_k(z)$. The reaction rate takes the form:

$$\begin{aligned} R(z) \;= k\, C_{O2}^{0} \Bigg(& \frac{C_{O2}(z)}{C_{O2}^{0}} \left(\frac{C_{O2}(z)}{C_{O2}^{0}} \right)^{1/8} \exp\left[-\frac{F}{2\, R\, T} (V_C(z) - V_P(z) - E_{0,c}) \right] \\ & - \left(\frac{C_{O2}(z)}{C_{O2}^{0}} \right)^{1/8} \exp\left[\frac{F}{2\, R\, T} (V_C(z) - V_P(z) - E_{0,c}) \right] \Bigg) \end{aligned} \tag{4.11}$$

where the standard potential for the ORR $E_{0,c} = 1.23$ V. As the backward reaction has a significant value only near the equilibrium (E_{Nernst}) where the oxygen is not depleted from the catalytic layer, the equation for the reaction rate is assumed to be:

$$\begin{aligned} R(z) \;= k\, C_{O2}^{0} \Bigg(& \left(\frac{C_{O2}(z)}{C_{O2}^{0}} \right)^{9/8} \exp\left[-\frac{F}{2\, R\, T} (V_C(z) - V_P(z) - E_{0,c}) \right] \\ & - \exp\left[\frac{F}{2\, R\, T} (V_C(z) - V_P(z) - E_{0,c}) \right] \Bigg) \end{aligned} \tag{4.12}$$

4.2.2 Oxygen, electrons and protons equations

Assuming an homogeneous catalytic layer of thickness H, the mass balance equation for oxygen can be written as:

$$D_{O2}\, d^2_{zz} C_{O2}(z) = R(z) \tag{4.13}$$

with D_{O2} being the diffusion coefficient inside the catalytic layer. The boundary conditions are:

$$d_z C_{O2}(z) = 0 \quad \text{for} \quad z = 0 \tag{4.14}$$

and

$$C_{O2}(z) = C^0_{O2} \quad \text{for} \quad z = H. \tag{4.15}$$

That means that there is no oxygen diffusion from/to the PEM and that the concentration at the inlet of the catalytic layer is equal to the feed of the electrode. The latter fixes the concentration at the inlet of the catalytic layer.

The current density of protons in the Nafion® is governed by Ohm's law:

$$J_P(z) = -\sigma_P\, d_z V_P(z) \tag{4.16}$$

where σ_P is the effective conductivity of protons in the Nafion®. Because of the reactions occurring throughout the catalytic layer, the current density is not constant and it obeys:

$$d_z J_P(z) = -4\, F\, R(z) \tag{4.17}$$

Combining these two equations leads to:

$$\sigma_P\, d^2_{zz} V_P(z) = 4\, F\, R(z) \tag{4.18}$$

with boundary conditions:

$$V_P(z) = 0 \quad \text{for} \quad z = 0 \tag{4.19}$$

and

$$d_z V_P(z) = 0 \quad \text{for} \quad z = H. \tag{4.20}$$

The former boundary condition takes the potential at the membrane as a reference assuming that there is no overpotential due to the anode reaction, the contact resistance at the anode and the membrane conductivity. The latter boundary condition imposes the proton current equal to zero at the GDL.

With a similar reasoning for the electron current density, J_C, than the one used for the proton current density, J_P, the potential of electrons in the carbon obeys:

$$\sigma_C\, d^2_{zz} V_C(z) = -4\, F\, R(z) \tag{4.21}$$

where σ_C is the effective conductivity of electrons in the carbon, with boundary conditions:

$$d_z V_C(z) = 0 \quad \text{for} \quad z = 0 \tag{4.22}$$

and

$$V_C(z) = V_C^0 \quad \text{for} \quad z = H. \tag{4.23}$$

The first boundary condition means that there is no electron flow in the PEM. The second boundary condition fixes the potential applied to the modeled fuel cell. V_C^0 is assumed to be the potential of the cathode and ignores all the contact resistances between the catalytic layer and the current collector.

4.2.3 Dimensionless equations

Let us now define the dimensionless version of our variables:

$$x = z/H \tag{4.24}$$

$$c(x) = C_{O2}/C_{O2}^0 \tag{4.25}$$

$$v_P(x) = \frac{F}{2\,R\,T} V_P \tag{4.26}$$

$$v_C(x) = \frac{F}{2\,R\,T} V_C \tag{4.27}$$

$$v_C^0(x) = \frac{F}{2\,R\,T} V_C^0 \tag{4.28}$$

$$v_{ref} = \frac{F}{2\,R\,T} E_{0,c} \tag{4.29}$$

$$r(x) = \frac{1}{k\,C_{O2}^0} R \tag{4.30}$$

The oxygen diffusion reaction becomes:

$$\begin{aligned} d_{xx}^2 c(x) &= \phi^2\, r(x) \\ &= \phi^2\, (c^{9/8}(x)\, \exp[-(v_C(x) - v_P(x) - v_{ref})] - \exp[v_C(x) - v_P(x) - v_{ref}]) \end{aligned} \tag{4.31}$$

with boundary conditions:

$$d_x c(x) = 0 \quad \text{for} \quad x = 0, \tag{4.32}$$

$$c(x) = 1 \quad \text{for} \quad x = 1 \tag{4.33}$$

and

$$\phi^2 = \frac{k\,H^2}{D_{O2}} \tag{4.34}$$

being the Thiele modulus. This dimensionless number is particularly convenient in our case as it used in a physicochemical system as the ratio between the reaction rate and the diffusion rate.

The dimensionless electrical potential in the Nafion® can be written as:

$$\begin{aligned} d^2_{xx} v_P(x) &= \frac{\phi^2}{\Sigma_P}\, r(x) \\ &= \frac{\phi^2}{\Sigma_P}\, (c^{9/8}(x)\, \exp[-(v_C(x) - v_P(x) - v_{ref})] - \exp[v_C(x) - v_P(x) - v_{ref}]) \end{aligned} \tag{4.35}$$

with boundary conditions:

$$v_P(x) = 0 \quad \text{for} \quad x = 0, \tag{4.36}$$

$$d_x v_P(x) = 0 \quad \text{for} \quad x = 1 \tag{4.37}$$

and

$$\Sigma_P = \frac{\sigma_P\, R\, T}{4\, F^2\, D_{02}\, C^0_{O2}} \tag{4.38}$$

Finally, the dimensionless electrical potential in the carbon is:

$$\begin{aligned} d^2_{xx} v_C(x) &= -\frac{\phi^2}{\Sigma_C}\, r(x) \\ &= -\frac{\phi^2}{\Sigma_C}\, (c^{9/8}(x)\, \exp[-(v_C(x) - v_P(x) - v_{ref})] - \exp[v_C(x) - v_P(x) - v_{ref}]) \end{aligned} \tag{4.39}$$

with boundary conditions:

$$d_x v_C(x) = 0 \quad \text{for} \quad x = 0, \tag{4.40}$$

$$v_C(x) = v^0_C \quad \text{for} \quad x = 1 \tag{4.41}$$

and

$$\Sigma_C = \frac{\sigma_C\, R\, T}{4\, F^2\, D_{02}\, C^0_{O2}} \tag{4.42}$$

The current model is constituted of three dimensionless parameters. Σ_P is the ratio between the proton conductivity and the diffusion coefficient of oxygen. Similarly, Σ_C compares the electron conductivity and the rate of diffusion of oxygen. ϕ is used to compare the influence of the reaction rate and the oxygen diffusion rate.

4.3 Numerical method

The three unknowns c, v_P and v_C are described by an equation of the type:

$$d^2_{xx}u = f(u) \tag{4.43}$$

where $f(u)$ a non-linear function. The only difficulty is the non-linearity of f which precludes a direct solution. A way to solve it is to use a relaxation approach [60]. This method consists in using a bogus time-dependent equation of the form:

$$\partial_t u = \partial_{xx}u - f(u) \tag{4.44}$$

and letting it run until the stationary state is reached to find the actual solution of Eq. 4.43.

Let us discretise space with $N+2$ nodes from $x=0$ to $x=1$, that is N nodes in the domain numbered $i=1,...,N$, and two on the boundaries. The Laplacian in the interior nodes is calculated using a finite-difference method:

$$\partial^2_{xx}u|_i = \frac{1}{\Delta x^2}(u_{i-1} - 2\,u_i + u_{i+1}) \tag{4.45}$$

with $\Delta x = 1/(N+1)$. The expressions of $\partial^2_{xx}u|_1$ and $\partial^2_{xx}u|_N$ can be calculated based on the boundary conditions of each unknown:

$$c: \quad \partial^2_{xx}c|_1 = \frac{1}{\Delta x^2}(-c_1 + c_2) \quad \partial^2_{xx}c|_N = \frac{1}{\Delta x^2}(c_{N-1} - 2c_N) + \frac{1}{\Delta x^2} \tag{4.46}$$

$$v_C: \quad \partial^2_{xx}v_C|_1 = \frac{1}{\Delta x^2}(-v_{C,1} + v_{C,2}) \quad \partial^2_{xx}v_C|_N = \frac{1}{\Delta x^2}(v_{C,N-1} - 2v_{C,N}) + \frac{v^0_C}{\Delta x^2} \tag{4.47}$$

with the gradient equal to zero at $x=0$ ($c_0 = c_1$, $v_{C,0} = v_{C,1}$) and the imposed value at $x=1$ ($c=1$, $v_C = v^0_C$), and

$$v_P: \quad \partial^2_{xx}v_P|_1 = \frac{1}{\Delta x^2}(-2v_{P,1} + v_{P,2}) \quad \partial^2_{xx}v_P|_N = \frac{1}{\Delta x^2}(v_{P,N-1} - v_{P,N}) \tag{4.48}$$

with $v_{P,0} = 0$ and $v_{P,N+1} = v_{P,N}$. The discretised equation can thus be written in a vector form as:

$$d_t U = D\,U + B - F \tag{4.49}$$

with U being the vector of unknowns:

$$U = \begin{bmatrix} u_1 \\ \vdots \\ u_N \end{bmatrix}. \tag{4.50}$$

The diffusion matrix has the form:

$$D_{c,vc} = \begin{bmatrix} -1 & 1 & & & \\ 1 & -2 & 1 & & \\ & \ddots & \ddots & \ddots & \\ & & 1 & -2 & 1 \\ & & & 1 & -2 \end{bmatrix} \tag{4.51}$$

for c and v_C, and

$$D_{vp} = \begin{bmatrix} -2 & 1 & & & \\ 1 & -2 & 1 & & \\ & \ddots & \ddots & \ddots & \\ & & 1 & -2 & 1 \\ & & & 1 & -1 \end{bmatrix} \tag{4.52}$$

for v_P. All the non-specified terms in the diffusion matrices are zero. The boundary condition vector is:

$$B_c = \begin{bmatrix} 0 \\ \vdots \\ 0 \\ \dfrac{1}{\Delta x^2} \end{bmatrix} \tag{4.53}$$

for c,

$$B_{vc} = \begin{bmatrix} 0 \\ \vdots \\ 0 \\ \dfrac{v_C^0}{\Delta x^2} \end{bmatrix} \tag{4.54}$$

for v_C and

$$B_{vp} = \begin{bmatrix} 0 \\ \vdots \\ 0 \end{bmatrix} \tag{4.55}$$

for v_P. Finally, the source vector is given by:

$$F = \begin{bmatrix} f(u_1) \\ \vdots \\ f(u_N) \end{bmatrix}. \tag{4.56}$$

The time-dependency in Eq. 4.49 is discretised using the implicit Euler scheme to ensure numerical stability:

$$\frac{1}{\Delta t}\left(U^{t+1} - U^t\right) = D\,U^{t+1} + B - F^t \tag{4.57}$$

which leads to:

$$U^{t+1} = [I - \Delta t D]^{-1} \left(U^t + \Delta t \left(B - F^t\right)\right). \tag{4.58}$$

where I is the identity matrix. The vector C will converge to the stationary solution by applying this equation recursively, starting from any reasonable guess.

4.4 Results and discussion

The results of the implementation of the 1D model with the parameters ϕ^2, Σ_P and Σ_C fixed at 1 are displayed in Fig. 4.2. The dimensionless open circuit potential v_{ref} is chosen as $F\,(1.23\,\mathrm{V})/2\,RT$, *i.e.* the standard potential for the ORR, and the cell potential v_C^0 is decreased from v_{ref} by steps of 2. As expected, decreasing the potential of the fuel cell increases the reaction rate and depletes the oxygen concentration near $x = 0$, *i.e.* the membrane side of the catalytic layer (Fig. 4.2a). One can see that the reaction rate increases also in this region to compensate the lack of reactants near the membrane (Fig. 4.2b). The effect of the variation of the cell potential on the potential of the protons and the electrons is given in Fig. 4.2c. The proton potential is more impacted from the depletion of oxygen. Indeed, as the protons arrive from the membrane side, the potential in the Nafion® needs a larger slope to carry the protons to the the active site near $x = 1$ where oxygen is still available. On the contrary, the carbon potential slope is barely dependent on the potential v_C^0 and on the depletion of oxygen as electrons are fed by the same side as oxygen and do not have to cross the layer to react.

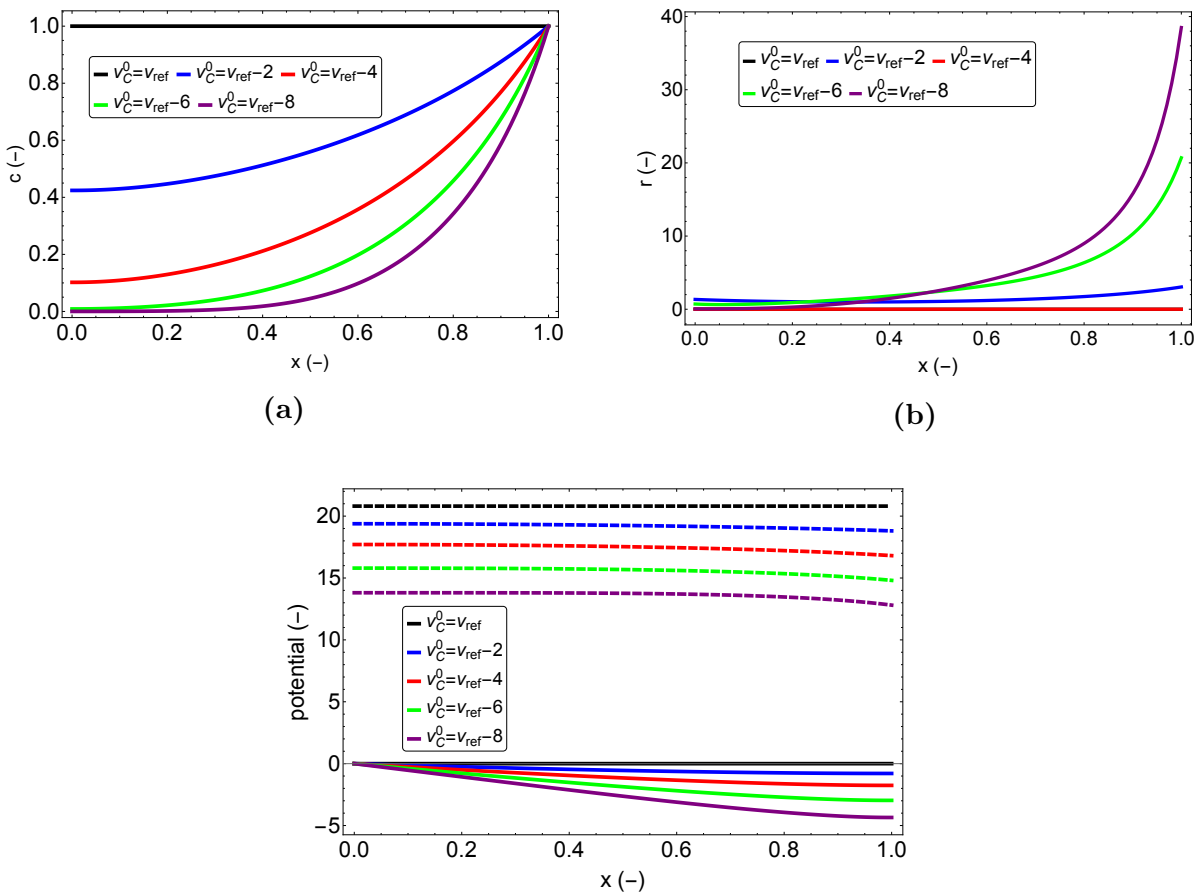

Figure 4.2: Dimensionless oxygen concentration c (a), reaction rate r (b), proton potential v_P (in solid lines) and electron potential v_C (in dashed lines) (c) as a function of the catalytic layer depth x. The dimensionless open circuit cell potential is $v_{ref} = F\,(1.23\,\mathrm{V})/2\,RT$ and the dimensionless cell potential v_C^0 is decreased from v_{ref} by steps of 2. The dimensionless parameters ϕ^2, Σ_P and Σ_C are fixed at 1.

When increasing the Thiele modulus, an increase of the number of active sites or a decrease of the diffusion constant inside the catalytic layer is performed. For a fixed cell potential v_C^0, the oxygen concentration is reduced more abruptly for $\phi^2 = 100$ than for $\phi^2 = 1$ due to the aforementioned reasons (Fig. 4.3a). A high Thiele modulus results in a large increase of the reaction rate as shown in Fig. 4.3b. Obviously, the situation is reversed for $\phi^2 = 0.01$ and the concentration in oxygen remains higher on the whole layer. The potential in the carbon and the Nafion® are impacted by the increase of the reaction. Finally, facilitating the proton transport by increasing the dimensionless conductivity in Nafion® Σ_P allows to consume more oxygen (Fig. 4.4). The layer is thus more depleted with $\Sigma_P = 100$ than $\Sigma_P = 1$ and $\Sigma_P = 0.01$ for a fixed cell potential v_C^0. For a smaller proton conductivity,

the reaction rate is forced to be increased next to the membrane where protons travel more easily.

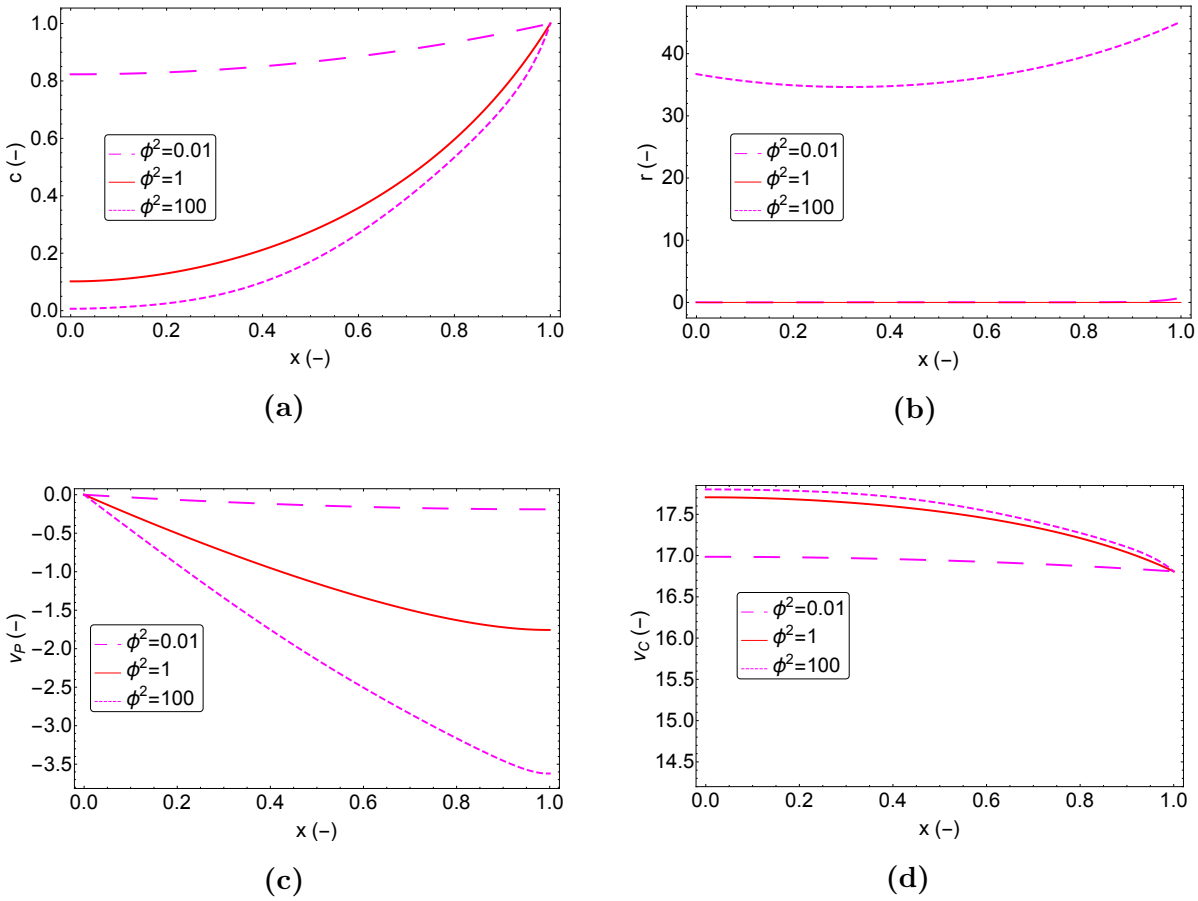

Figure 4.3: Dimensionless oxygen concentration c (a), reaction rate r (b), proton potential v_P (c) and electron potential v_C (d) as a function of the catalytic layer depth x. The dimensionless open circuit cell potential v_{ref} is $F\,(1.23\,\mathrm{V})/2\,RT$ and the cell potential v_C^0 is fixed at $v_{ref} - 4$. The Thiele modulus ϕ^2 takes the values 0.01, 1 and 100 while Σ_P and Σ_C are equal to 1.

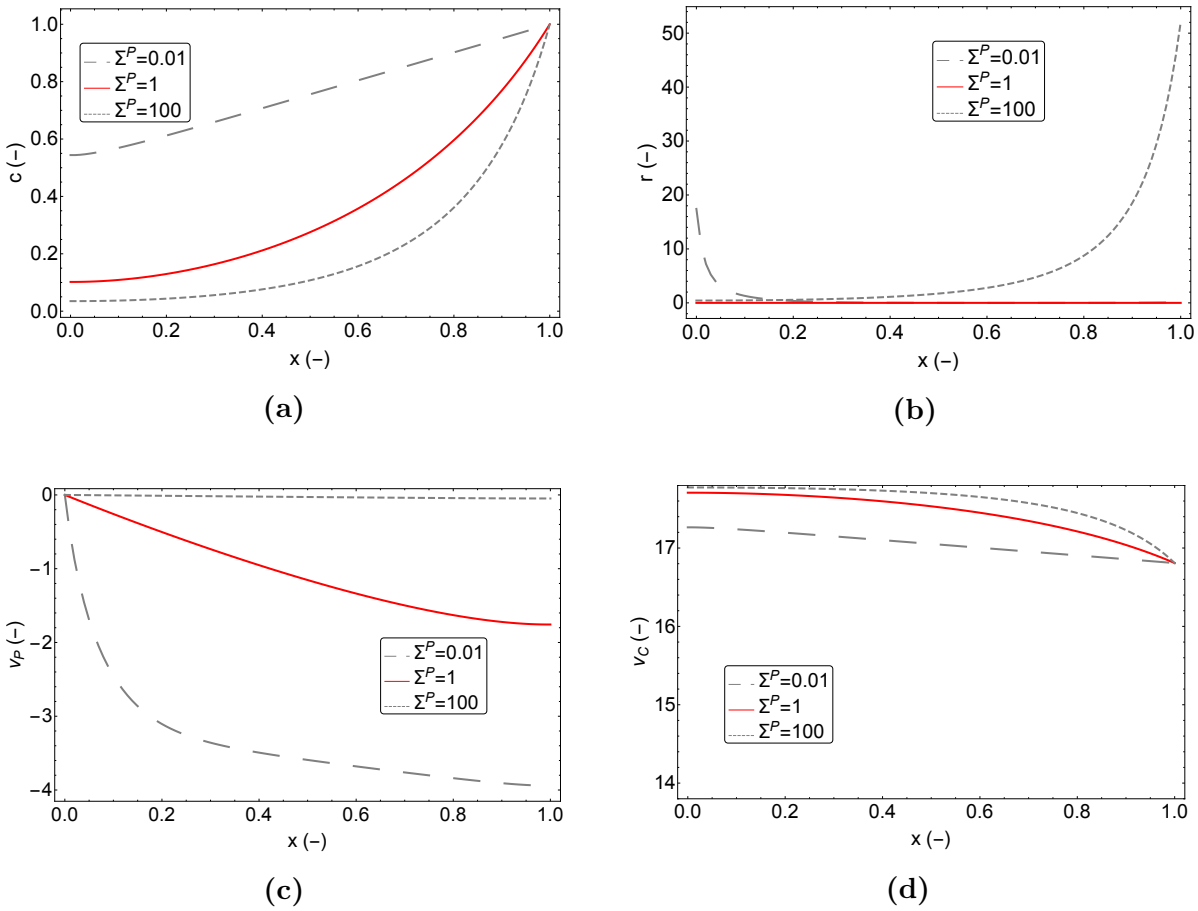

Figure 4.4: Dimensionless oxygen concentration c(a), reaction rate r (b), proton potential v_P (c) and electron potential v_C (d) as a function of the catalytic layer depth x. The dimensionless open circuit cell potential v_{ref} is $F\,(1.23\,\mathrm{V})/2\,RT$ and the cell potential v_C^0 is $v_{ref} - 4$. The dimensionless proton conductivity Σ_P takes the values 0.01, 1 and 100 while ϕ^2 and Σ_C are equal to 1.

The model polarisation curves can also be computed by looping on the values of the cell potential, *i.e.* the electric potential at the right boundary of the domain v_C^0. The values chosen to display the polarisation curves start at the open circuit voltage, $F\,(1.23\,\mathrm{V})/2\,RT$, and decrease to obtain a current. The relation involving the dimensionless current in the model is adapted from Eq. 4.17:

$$d_x j_C = -d_x j_P = r \tag{4.59}$$

The value of the current is computed by integrating the right hand side of the equation. As the reaction rate R is normalised by the exchange reaction ($k\,C_{O2}^0$) to give r, the dimensionless currents j_C and j_P are the values of the currents normalised by the exchange current.

The carbon support is usually carbon black in PEM fuel cells. The electric conductivity is therefore not a limiting parameter of the system and Σ_C can be reasonably chosen equal to 100 to compute the following polarisation curves (Fig. 4.5). The performance increases when ϕ^2 decreases due to the fact that the diffusion coefficient increases. As a result, the oxygen is less depleted from the catalytic layer. One can also see that, for a small value of the proton conductivity ($\Sigma_P = 0.01$), the current density tend to reach a limit at low cell voltage. This indicates that the proton conductivity is the larger limitation factor in this model as this limiting current is not reached for the same value of the voltage when Σ_P increases.

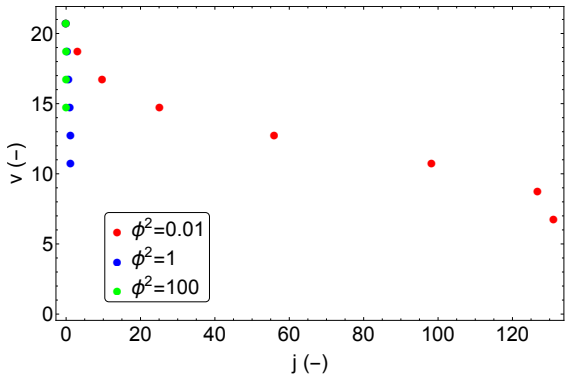

(a) $\Sigma_P = 0.01$

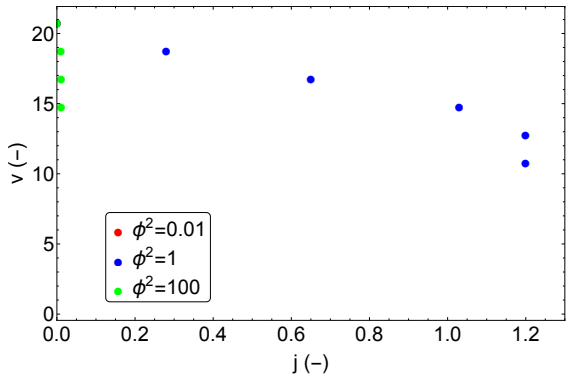

(b) $\Sigma_P = 0.01$, zoom on lower currents

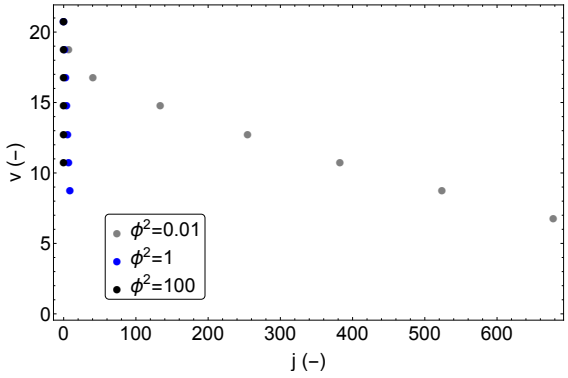

(c) $\Sigma_P = 1$

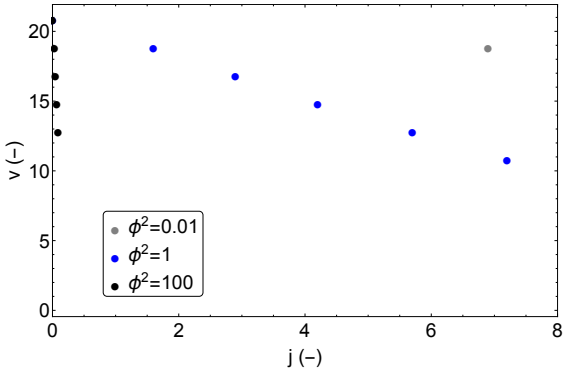

(d) $\Sigma_P = 1$, zoom on lower currents

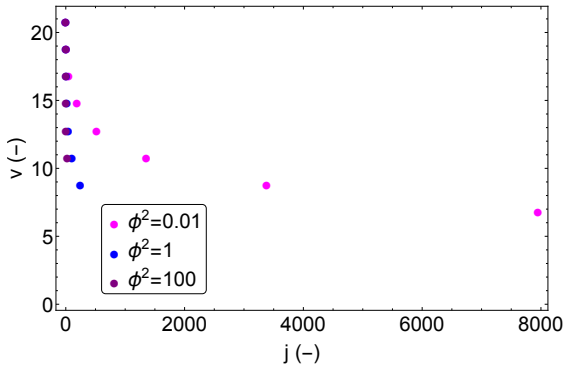

(e) $\Sigma_P = 1$

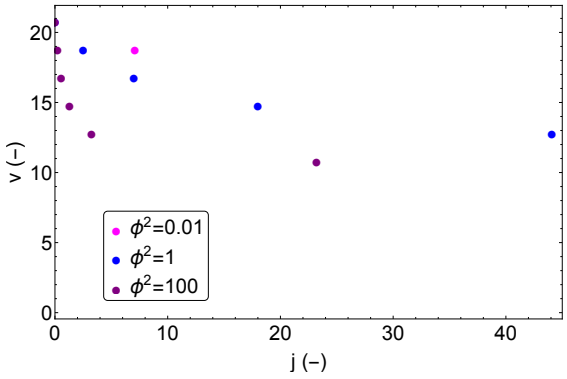

(f) $\Sigma_P = 1$, zoom on lower currents

Figure 4.5: Polarisation curves obtained with the cathode catalytic model for $\Sigma_C = 100$, (a,b) $\Sigma_P = 0.01$ (c,d) $\Sigma_P = 1$ (e,f) $\Sigma_P = 100$ and various values of ϕ^2.

4.5 Model fitting

The results from the characterisation of complete PEM fuel cells (Chapter 3) can now be used to fit the present model. As the modelling dealt only with the cathode catalytic layer, the overpotential related to the other parts of the fuel cell should be retrieved before the fitting. During the experimental characterisations, the catalyst loading at the anode was fixed at a high value. The contribution of this part of the cell to the overpotential can thus be neglected thanks to the fast kinetic of the hydrogen oxidation reaction [18] and the fast diffusion of hydrogen. The membrane and contact resistance of the device R_{el} has a significant value and could be found by impedance spectroscopy. A Ohm's law of the following form:

$$E = R_{el}\, i \tag{4.60}$$

is applied to the potential E of the experimental polarisation curve in accordance with the equivalent circuit model (Chapter 3).

The values for the parameters involved in the definition of ϕ^2, Σ_P and Σ_C are summarised in Table 4.1. The concentration at the inlet is computed from the ideal gas' law:

$$C^0_{O2} = \frac{P\,\chi_{O2}}{R\,T} \tag{4.61}$$

with $P = 50$ kPa being the pressure in the oxygen gas line and $\chi_{O2} = 0.2$ is the mole fraction of oxygen in the air used to supply the cell. The Nafion® ionic conductivity and carbon electric conductivity were obtained from previous experiments at the laboratory. The unknown parameter k is the degree of freedom for the fitting. The fitted dimensionless parameters are:

$$\phi^2 = 8.2\,10^{-3} \qquad \Sigma_P = 1.27 \qquad \Sigma_C = 41.1 \tag{4.62}$$

While the fitting and the experimental curves at low current tends to the same behaviour, the model fails to get the limiting current associated to the diffusion losses at higher current (Fig. 4.6). This could be explained by the simple model used in the context of this project. The oxygen is the only gas reactant considered and the effect of the nitrogen and the water are neglected. Also, in this chapter, the bipolar plates and gas diffusion layers are not modeled even though they impact the performance of the fuel cell. The transition to a 2D model involving those components of the fuel cell could give a better fit.

Table 4.1: Values of the parameters used for the fitting of the model on the experimental polarisation curve. The unknown parameter k is the degree of freedom.

Parameter	Value
Temperature T	343 K
Catalytic layer width H	10 μm
Nafion® ionic conductivity σ_P	0.028 $(\Omega\,\mathrm{cm})^{-1}$
Carbon electric conductivity σ_C	0.917 $(\Omega\,\mathrm{cm})^{-1}$
Catalytic layer porosity ϵ	0.46
Diffusion coefficient D_{O2}	$\epsilon^2 \times 0.23$ cm^2 s^{-1}

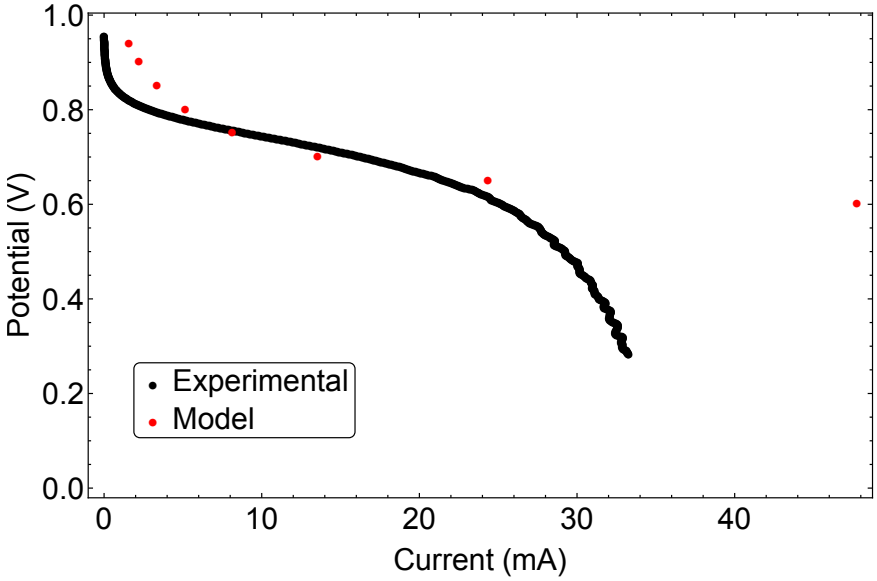

Figure 4.6: Polarisation curves obtained during the experiments conducted at the laboratory (EMEb-2) (Chapter 3) and the model with fitted parameters of Table 4.1.

4.6 Conclusion

In this last chapter, the aim was to study the limitations of the cathode catalytic layer through a 1D pseudo homogeneous model. To that end, the reaction rate of the oxygen reduction reaction was derived from Butler-Volmer equation. The transport of the protons and electrons was modeled with a Ohm's law while the oxygen diffusion phenomenon in the electrode was retrieved using a Fick's law. The dependence of the reaction rate with respect of the catalytic layer depth was assessed. Also, the influence of the physico-chemical parameters through the dimensionless numbers (ϕ^2 and Σ_P) on the performance was described. For a small value of Σ_P, a limiting current was reached at low potential which corresponds to realistic curves. The model was eventually used to fit the experimental data previously acquired at the laboratory. While the performance of the model at low current tends to the right behaviour, the current-potential deviates at high current, never reaching the current plateau. This indicates that the model still fails to reconstruct the real behaviour of the PEM fuel cell due to its simplicity.

GENERAL CONCLUSION

In this master thesis, we were interested in the origins of the drop in performance on the cathodic side of the PEM fuel cell. To that end, catalytic layers with different compostions were planned to be considered in order to dissociate the performance loss due to the transport of the various species (electrons, protons and gas).

The experimental approach of the PEM fuel cells was first considered. Platinum on carbon black was synthesised using the formic acid impregnation method, *i.e.* a technique consisting in reducing directly the Pt precursor in liquid phase during the impregnation of the support. This catalyst was characterised using physical (XRD, TEM) and electrochemical techniques (CO stripping, RDE) to evaluate the sizes and the activity of the deposited Pt particles. The activity values from RDE were similar to what is encountered in the literature. The crystallite size given by XRD and the average diameter obtained with CO stripping were of the order of 3 to 5 nm. However, TEM showed that the Pt particles formed agglomerates on the carbon support certainly due to a too fast Pt salt injection during the synthesis by impregnation-reduction.

The manufacture process of the PEM fuel cell was then tackled. Catalyst coated membranes were made by robot spray deposition using a commercial Pt/C catalyst. A larger Pt loading was set on the anode side (0.81 mg cm^{-2} > 0.13 mg cm^{-2}) in order to study the limitations at the cathode electrode only. The reproducibility of the fabrication as well as two conditioning processes were validated with *in situ* techniques. The final performance reached by the fuel cells showed that none of the conditioning techniques were able to speed up the activation process satisfactorily. The reproducibility was enhanced from the first set of fuel cells to the second. The increase of the spray flow rate during the robot spray deposition is suspected to be the reason for this improvement. The excellent reproducibility reached

with the second set of the fuel cells would have been sufficient to highlight the limitations of catalytic layer architectures.

As pursuing the experimental work was made impossible due to the 2020 health crisis, a 1D model was finally developed to simulate the PEM fuel cell performance. The model deals with the cathode catalytic layer. The medium was assumed to be homogeneous: constant diffusion coefficient, electric and ionic conductivity along the layer were utilised. The model could highlight the dependence of the reaction rate, the concentration of gas reactants and the potentials with respect to the physical parameters of the catalytic layer. The predicted performance tends to the behaviour obtained with the experimental data at low current but failed to retrieve the concentration losses at high current. This result is not surprising as the model considers a macroscopic diffusion of the gas reactant and neglects the effect of other components such as the GDL and the bipolar plates.

Outlook

First of all, in order to continue the project and to manufacture PEM fuel cells with catalytic layers of various composition, being table to synthesise reproducible and homogeneous catalyst is essential. The Pt salt injection during the synthesis could be performed using a syringe pump to control the flowrate and to avoid catalyst agglomerates.

In view of the results obtained in the Chapter 3 where the PEM fuel cells were manufactured and characterised on the fuel cell test bench, some other experiments could be conducted to enhance both the conditioning and the reproducibility of the PEM fuel cell. As an activation process, a technique based on gas supply with higher pressure than the operating pressure have been reported as efficient [41] and could be used combined with other techniques [39] for next experiments.

In order to have a better reproducibility, some of the components of the PEM fuel cell could be characterised. As the GDL is not made at the laboratory, its fabrication process is unknown although it could impact the properties of the GDL such as the electric conductivity. It should be verified that the conductivity of the GDLs are equal and that the material conductivity is isotropic and does not have a preferential direction. Furthermore, the impact of the temperature and humidity change inside the robot spray container could be assessed by characterising the spray deposition. Profilometry, as described by Deschamps *et al.* [44], seems to be a relevant choice to evaluate the topography. A clear procedure to obtain reproducible spray depositions on the PEM could then be set up. Also, the increase

in thickness of the gaskets requires a larger value of the force applied during the hot pressing. This could ensure a better contact between the catalytic layer and the GDL and decrease the ohmic resistance of the fuel cells. Finally, even though enhancements are possible, the reproduciblity obtained with the second set of fuel cells is sufficient to compare devices with different catalyst compositions and continue the experimental project. Indeed, the following step of the experimental project is the manufacture of PEM fuel cells where the catalyst is situated only close to the proton exchange membrane and, the opposite case, where the Pt particles are only close to the oxygen supply.

The 1D model from Chapter 4 could be further developed in order to fit the data acquired experimentally. For that purpose, the physical parameters of the catalytic layers such as the ionic and the electric conduction could be retrieved at the laboratory. A more elaborated diffusion behaviour inside the catalytic layer could also be implemented. The diffusion process could involve the nitrogen and the water. The introduction of the stoechiometry parameter related to the flow rates of the gas reactants could similarly improve the correctness of the model. All these proposals will be considered in future works at the NCE laboratory.

REFERENCES

[1] N. Guerrero Moreno, M. Cisneros Molina, D. Gervasio, and J. F. Pérez Robles, "Approaches to polymer electrolyte membrane fuel cells (PEMFCs) and their cost," *Renewable and Sustainable Energy Reviews*, vol. 52, pp. 897–906, 8 2015.

[2] O. Z. Sharaf and M. F. Orhan, "An overview of fuel cell technology: Fundamentals and applications," *Renewable and Sustainable Energy Reviews*, vol. 32, pp. 810–853, 4 2014.

[3] F. Barbir, *PEM Fuel Cell Theory and practice*. Elsevier, 2005.

[4] J. Smith, M. Nehrir, V. Gerez, and S. Shaw, "A broad look at the workings, types, and applications of fuel cells," *IEEE Power Engineering Society Summer Meeting*, pp. 70–75, 2002.

[5] A. Coralli, B. J. Sarruf, P. E. V. De Miranda, L. Osmieri, S. Specchia, and N. Q. Minh, "Fuel cells," in *Science and Engineering of Hydrogen-Based Energy Technologies: Hydrogen Production and Practical Applications in Energy Generation*, pp. 39–122, Elsevier, 1 2018.

[6] G. Merle, M. Wessling, and K. Nijmeijer, "Anion exchange membranes for alkaline fuel cells: A review," *Journal of Membrane Science*, vol. 377, pp. 1–35, 7 2011.

[7] O. Erdinc and M. Uzunoglu, "Recent trends in PEM fuel cell-powered hybrid systems: Investigation of application areas, design architectures and energy management approaches," *Renewable and Sustainable Energy Reviews*, vol. 14, no. 9, pp. 2874–2884, 2010.

[8] T. S. Zhao, K.-D. Kreuer, and T. V. Nguyn, *Advances in fuel cells*. Elsevier, 2007.

[9] V. Mehta and J. S. Cooper, "Review and analysis of PEM fuel cell design and manufacturing," *Journal of Power Sources*, vol. 114, pp. 32–53, 2003.

[10] A. V. Anantaraman, "Studies on ion-exchange membranes. Part 1. Effect of humidity on the conductivity of Nafion"," *Journal of Electroanalytical Chemistry*, vol. 414, pp. 115–120, 1996.

[11] K. Scott, "Membrane electrode assemblies for polymer electrolyte membrane fuel cells," in *Functional materials for sustainable energy applications*, ch. 10, pp. 279–311, Woodhead, 2012.

[12] J. Zhang, *PEM Fuel Cell Electrocatalysts and Catalyst Layers*. 2008.

[13] S. Jeon, J. Lee, G. M. Rios, H. J. Kim, S. Y. Lee, E. Cho, T. H. Lim, and J. Hyun Jang, "Effect of ionomer content and relative humidity on polymer electrolyte membrane fuel cell (PEMFC) performance of membrane-electrode assemblies (MEAs) prepared by decal transfer method," *International Journal of Hydrogen Energy*, vol. 35, pp. 9678–9686, 9 2010.

[14] H. Li, Y. Tang, Z. Wang, Z. Shi, S. Wu, D. Song, J. Zhang, K. Fatih, J. Zhang, H. Wang, Z. Liu, R. Abouatallah, and A. Mazza, "A review of water flooding issues in the proton exchange membrane fuel cell," *Journal of Power Sources*, vol. 178, pp. 103–117, 3 2008.

[15] A. Hermann, T. Chaudhuri, and P. Spagnol, "Bipolar plates for PEM fuel cells: A review," in *International Journal of Hydrogen Energy*, vol. 30, pp. 1297–1302, 9 2005.

[16] A. J. Bard and L. R. Faulkner, *Electrochemical methods : fundamentals and applications*. Wiley, 2001.

[17] J. Zhang, Y. Tang, C. Song, J. Zhang, and H. Wang, "PEM fuel cell open circuit voltage (OCV) in the temperature range of 23 °C to 120 °C," *Journal of Power Sources*, vol. 163, pp. 532–537, 12 2006.

[18] C. Song, Y. Tang, J. L. Zhang, J. Zhang, H. Wang, J. Shen, S. McDermid, J. Li, and P. Kozak, "PEM fuel cell reaction kinetics in the temperature range of 23-120 °C," *Electrochimica Acta*, vol. 52, pp. 2552–2561, 2 2007.

[19] J. Kim, "Modeling of Proton Exchange Membrane Fuel Cell Performance with an Empirical Equation," *Journal of The Electrochemical Society*, vol. 142, no. 8, p. 2670, 1995.

[20] L. Pisani, G. Murgia, M. Valentini, and B. D'aguanno, "A new semi-empirical approach to performance curves of polymer electrolyte fuel cells," *Journal of Power Sources*, vol. 108, pp. 192–203, 2002.

[21] H. K. Lee, J. H. Park, D. Y. Kim, and T. H. Lee, "A study on the characteristics of the diffusion layer thickness and porosity of the PEMFC," *Journal of Power Sources*, vol. 131, pp. 200–206, 5 2004.

[22] H. A. Gasteiger, J. E. Panels, and S. G. Yan, "Dependence of PEM fuel cell performance on catalyst loading," in *Journal of Power Sources*, vol. 127, pp. 162–171, 3 2004.

[23] K. Kinoshita, "Particle Size Effects for Oxygen Reduction on Highly Dispersed Platinum in Acid Electrolytes," *Ber. Bunsenges. Physik. Chem*, vol. 137, no. 3, p. 147, 1990.

[24] O. Antoine, Y. Bultel, and R. Durand, "Oxygen reduction reaction kinetics and mechanism on platinum nanoparticles inside Nafion ®," *Journal of Electroanalytical Chemistry*, vol. 499, pp. 85–94, 2001.

[25] F. Maillard, N. Job, and M. Chatenet, "Approaches to Synthesize Carbon-Supported Platinum-Based Electrocatalysts for Proton-Exchange Membrane Fuel Cells," in *New and Future Developments in Catalysis: Batteries, Hydrogen Storage and Fuel Cells*, pp. 407–428, Elsevier B.V., 2013.

[26] A. Zubiaur and N. Job, "Streamlining of the synthesis process of Pt/carbon xerogel electrocatalysts with high Pt loading for the oxygen reduction reaction in proton exchange membrane fuel cells applications," *Applied Catalysis B: Environmental*, vol. 225, pp. 364–378, 6 2018.

[27] C. Alegre, M. E. Gálvez, R. Moliner, V. Baglio, A. S. Aricò, and M. J. Lázaro, "Towards an optimal synthesis route for the preparation of highly mesoporous carbon xerogel-supported Pt catalysts for the oxygen reduction reaction," *Applied Catalysis B: Environmental*, vol. 147, pp. 947–957, 4 2014.

[28] B. Cullity, S. Stock, and N. E. Bowie, *Elements of X-Ray Diffraction*. Pearson New International edition., 2014.

[29] F. Maillard, S. Schreier, M. Hanzlik, E. R. Savinova, S. Weinkauf, and U. Stimming, "Influence of particle agglomeration on the catalytic activity of carbon-supported Pt nanoparticles in CO monolayer oxidation," *Physical Chemistry Chemical Physics*, pp. 375–383, 2005.

[30] J. Zhang, H. Zhang, J. Wu, J. Zhang, A. L. Boston, H. L. London, N. York, P. L. San, D. San, F. L. Singapore, and S. L. Tokyo, *PEM Fuel Cell Testing and Diagnosis*. 2013.

[31] S. Gates-Rector and T. Blanton, "The Powder Diffraction File: A Quality Materials Characterization Database," 2019.

[32] N. Job, S. Lambert, M. Chatenet, C. J. Gommes, F. Maillard, S. Berthon-Fabry, J. R. Regalbuto, and J. P. Pirard, "Preparation of highly loaded Pt/carbon xerogel catalysts for Proton Exchange Membrane fuel cells by the Strong Electrostatic Adsorption method," *Catalysis Today*, vol. 150, pp. 119–127, 2 2010.

[33] E. Antolini, "Carbon supports for low-temperature fuel cell catalysts," *Applied Catalysis B: Environmental*, vol. 88, pp. 1–24, 4 2009.

[34] J. H. Wee, K. Y. Lee, and S. H. Kim, "Fabrication methods for low-Pt-loading electrocatalysts in proton exchange membrane fuel cell systems," *Journal of Power Sources*, vol. 165, pp. 667–677, 3 2007.

[35] I. S. Park, W. Li, and A. Manthiram, "Fabrication of catalyst-coated membrane-electrode assemblies by doctor blade method and their performance in fuel cells," *Journal of Power Sources*, vol. 195, pp. 7078–7082, 10 2010.

[36] M. Ahn, Y.-H. Cho, N. Jung, J. W. Lim, Y. S. Kang, and Y.-E. Sung, "Structural Modification of a Membrane Electrode Assembly via a Spray Coating in PEMFCs," *Journal of The Electrochemical Society*, vol. 159, no. 2, pp. B145–B149, 2011.

[37] A. M. Chaparro, B. Gallardo, M. A. Folgado, A. J. Martín, and L. Daza, "PEMFC electrode preparation by electrospray: Optimization of catalyst load and ionomer content," *Catalysis Today*, vol. 143, pp. 237–241, 5 2009.

[38] R. R. Passos, V. A. Paganin, and E. A. Ticianelli, "Studies of the performance of PEM fuel cell cathodes with the catalyst layer directly applied on Nafion membranes," *Electrochimica Acta*, vol. 51, pp. 5239–5245, 7 2006.

[39] Z. Xu, Z. Qi, C. He, and A. Kaufman, "Combined activation methods for proton-exchange membrane fuel cells," *Journal of Power Sources*, vol. 156, pp. 315–320, 6 2006.

[40] X. Z. Yuan, S. Zhang, J. C. Sun, and H. Wang, "A review of accelerated conditioning for a polymer electrolyte membrane fuel cell," *Journal of Power Sources*, vol. 196, pp. 9097–9106, 11 2011.

[41] Z. Qi and A. Kaufman, "Activation of low temperature PEM fuel cells," *Journal of Power Sources*, vol. 111, pp. 181–184, 2002.

[42] H. Voss, R. Barton, M. Sexsmith, and M. Turchyn, "Conditioning and maintenance methods for fuel cells," 2002.

[43] T. Lim, S. Kim, S. Ahn, B. Hong, and B. Ahn, "System and method for activating fuel cell," 2010.

[44] F. L. Deschamps, J. G. Mahy, A. F. Léonard, S. D. Lambert, A. Dewandre, B. Scheid, and N. Job, "A practical method to characterize proton exchange membrane fuel cell catalyst layer topography: Application to two coating techniques and two carbon supports," *Thin Solid Films*, vol. 695, pp. 1–14, 2 2020.

[45] H. A. Gasteiger, S. S. Kocha, B. Sompalli, and F. T. Wagner, "Activity benchmarks and requirements for Pt, Pt-alloy, and non-Pt oxygen reduction catalysts for PEMFCs," *Applied Catalysis B: Environmental*, vol. 56, pp. 9–35, 3 2005.

[46] A. Therdthianwong, P. Manomayidthikarn, and S. Therdthianwong, "Investigation of membrane electrode assembly (MEA) hot-pressing parameters for proton exchange membrane fuel cell," *Energy*, vol. 32, no. 12, pp. 2401–2411, 2007.

[47] M. B. Sassin, Y. Garsany, R. W. Atkinson, R. M. Hjelm, and K. E. Swider-Lyons, "Understanding the interplay between cathode catalyst layer porosity and thickness on transport limitations en route to high-performance PEMFCs," *International Journal of Hydrogen Energy*, vol. 44, pp. 16944–16955, 6 2019.

[48] O. Okur, Iyigün Karadağ, F. G. Boyaci San, E. Okumuş, and G. Behmenyar, "Optimization of parameters for hot-pressing manufacture of membrane electrode assembly for PEM (polymer electrolyte membrane fuel cells) fuel cell," *Energy*, vol. 57, pp. 574–580, 8 2013.

[49] S. Kim, S. Shimpalee, and J. W. Van Zee, "The effect of stoichiometry on dynamic behavior of a proton exchange membrane fuel cell (PEMFC) during load change," *Journal of Power Sources*, vol. 135, pp. 110–121, 9 2004.

[50] S. Kaytakoğlu and L. Akyalçin, "Optimization of parametric performance of a PEMFC," *International Journal of Hydrogen Energy*, vol. 32, pp. 4418–4423, 12 2007.

[51] B. G. Pollet, "A novel method for preparing PEMFC electrodes by the ultrasonic and sonoelectrochemical techniques," *Electrochemistry Communications*, vol. 11, pp. 1445–1448, 7 2009.

[52] R. Cuccaro, M. Lucariello, A. Battaglia, and A. Graizzaro, "Research of a HySyLab internal standard procedure for single PEMFC," *International Journal of Hydrogen Energy*, vol. 33, pp. 3159–3166, 6 2008.

[53] M. S. Mamat, S. A. Grigoriev, K. A. Dzhus, D. M. Grant, and G. S. Walker, "The performance and degradation of Pt electrocatalysts on novel carbon carriers for PEMFC applications," *International Journal of Hydrogen Energy*, vol. 35, pp. 7580–7587, 7 2010.

[54] M. G. Santarelli and M. F. Torchio, "Experimental analysis of the effects of the operating variables on the performance of a single PEMFC," *Energy Conversion and Management*, vol. 48, pp. 40–51, 1 2007.

[55] X.-Z. Yuan, C. Song, H. Wang, and J. Zhang, *Electrochemical Impedance Spectroscopy in PEM Fuel Cells: Fundamentals and Applications*. 2010.

[56] F. Liu, B. Yi, D. Xing, J. Yu, Z. Hou, and Y. Fu, "Development of novel self-humidifying composite membranes for fuel cells," *Journal of Power Sources*, vol. 124, pp. 81–89, 10 2003.

[57] X. Yu and S. Ye, "Recent advances in activity and durability enhancement of Pt/C catalytic cathode in PEMFC. Part II: Degradation mechanism and durability enhancement of carbon supported platinum catalyst," *Journal of Power Sources*, vol. 172, pp. 145–154, 10 2007.

[58] H. S. Park, Y. H. Cho, Y. H. Cho, C. R. Jung, J. H. Jang, and Y. E. Sung, "Performance enhancement of PEMFC through temperature control in catalyst layer fabrication," *Electrochimica Acta*, vol. 53, pp. 763–767, 12 2007.

[59] L. You and H. Liu, "A parametric study of the cathode catalyst layer of PEM fuel cells using a pseudo-homogeneous model," *International Journal of Hydrogen Energy*, vol. 26, pp. 991–999, 2001.

[60] T. Pang, "Partial differential equations," in *An Introduction to Computational Physics* (Cambridge, ed.), ch. 7, 2006.